minerals

MDPI

Article

Volcanic Response to Post-Pan-African Orogeny Delamination: Insights from Volcanology, Precise U-Pb Geochronology, Geochemistry, and Petrology of the Ediacaran Ouarzazate Group of the Anti-Atlas, Morocco

Mohamed Achraf Mediany [1], Nasrrddine Youbi [1,2,3,*], Mohamed Ben Chra [4], Oussama Moutbir [1], Ismail Hadimi [1], João Mata [2], Jörn-Frederik Wotzlaw [5], José Madeira [2], Miguel Doblas [6], Ezz El Din Abdel Hakim Khalaf [7], Rachid Oukhro [1], Warda El Moume [1], Jihane Ounar [1], Abdelhak Ait Lahna [8], Moulay Ahmed Boumehdi [1,2] and Andrey Bekker [9,10]

[1] Department of Geology, Faculty of Sciences-Semlalia, Cadi Ayyad University, Prince Moulay Abdellah Boulevard, P.O. Box 2390, Marrakesh 40000, Morocco; m.mediany.ced@uca.ac.ma (M.A.M.); o.moutbir.ced@uca.ac.ma (O.M.); ismail.hadimi@gmail.com (I.H.); oukhro.rachid@gmail.com (R.O.); warda.elmoume@gmail.com (W.E.M.); jihaneounar@gmail.com (J.O.); boumehdi@uca.ac.ma (M.A.B.)
[2] Instituto Dom Luiz, Faculdade de Ciências, Universidade de Lisboa, 1749-016 Lisboa, Portugal; jmata@ciencias.ulisboa.pt (J.M.); jmadeira@ciencias.ulisboa.pt (J.M.)
[3] Faculty of Geology and Geography, Tomsk State University, 36 Lenin Ave, Tomsk 634050, Russia
[4] Institute of Mines of Marrakech, Rue Machaar El Haram Quartier Issil, Marrakech 40000, Morocco; mbenchra5@gmail.com
[5] Institute of Geochemistry and Petrology, ETH Zürich, CH-8092 Zürich, Switzerland; joern.wotzlaw@gmail.com
[6] Indepedent Researcher, Tres Cantos, 28036 Madrid, Spain; mdoblaslavigne@gmail.com
[7] Faculty of Science Geology Department, Cairo University, Giza 12613, Egypt; ezzkhalaf2020@gmail.com
[8] Department of Geology, Faculty of Sciences, Ibn Zohr University, Agadir 80000, Morocco; aitlahna.abdelhak@gmail.com
[9] Department of Earth and Planetary Sciences, University of California, Riverside, CA 92521, USA; andreyb@ucr.edu
[10] Department of Geology, University of Johannesburg, Auckland Park, Johannesburg 2006, South Africa
* Correspondence: youbi@uca.ac.ma

Academic Editors: Ilya Bindeman and Ioan Seghedi

Received: 9 December 2024
Revised: 14 January 2025
Accepted: 27 January 2025
Published: 31 January 2025

Citation: Mediany, M.A.; Youbi, N.; Ben Chra, M.; Moutbir, O.; Hadimi, I.; Mata, J.; Wotzlaw, J.-F.; Madeira, J.; Doblas, M.; El Din Abdel Khalaf, E.E.D.A.H.; et al. Volcanic Response to Post-Pan-African Orogeny Delamination: Insights from Volcanology, Precise U-Pb Geochronology, Geochemistry, and Petrology of the Ediacaran Ouarzazate Group of the Anti-Atlas, Morocco. *Minerals* **2025**, *15*, 142. https://doi.org/10.3390/min15020142

Abstract: Post-collisional volcanism provides valuable insights into mantle dynamics, crustal processes, and mechanisms driving orogen uplift and collapse. This study presents geological, geochemical, and geochronological data for Ediacaran effusive and pyroclastic units from the Taghdout Volcanic Field (TVF) in the Siroua Window, Anti-Atlas Belt. Two eruptive cycles are identified based on volcanological and geochemical signatures. The first cycle comprises a diverse volcanic succession of basalts, basaltic andesites, andesites, dacites, and rhyolitic crystal-rich tuffs and ignimbrites, exhibiting arc calc-alkaline affinities. These mafic magmas were derived from a lithospheric mantle metasomatized by subduction-related fluids and are associated with the gravitational collapse of the Pan-African Orogen. The second cycle is marked by bimodal volcanism, featuring tholeiitic basalts sourced from the asthenospheric mantle and felsic intraplate magmas. These units display volcanological characteristics typical of facies models for continental basaltsuccessions and continental felsic volcanoes.s. Precise CA-ID-TIMS U-Pb zircon dating constrains the volcanic activity to 575–557 Ma, reflecting an 18-million-year period of lithospheric thinning, delamination, and asthenospheric upwelling. This progression marks the transition from orogen collapse to continental rifting, culminating in the breakup of the Rodinia supercontinent and the opening of the Iapetus Ocean. The TVF

exemplifies the dynamic interplay between lithospheric and asthenospheric processes during post-collisional tectonic evolution.

Keywords: Anti-Atlas; Ediacaran; volcanology; U-Pb geochronology

1. Introduction

Magmas associated with continental collisional orogens can be subdivided into pre-collisional, syn-collisional, and post-collisional [1–4]. Pre-collisional magmatism takes place during oceanic subduction, forming continental arcs similar to the modern Andean system. Syn-collisional magmatism occurs during continental collision, deep subduction, and exhumation, often coinciding with ultrahigh-pressure metamorphism 5 to 10 million years later, potentially resulting from decompressional melting of the earlier subducted continental crust [2,4]. Post-collisional magmatism marks the end of the Wilson cycle and signals the beginning of anorogenic within-plate tectonic setting, corresponding to the unroofing, collapse, and extension of the orogenic belt.

The Neoproterozoic to early Cambrian breakup of Rodinia led to separation of Laurentia, Baltica, and Amazonia/West Africa. It was associated with large igneous provinces (LIPs), protracted multiphase rifting, and variable subsidence along continental margin segments (e.g., [5] and references therein). The 620–520 Ma Central Iapetus Magmatic Province (CIMP) was emplaced in multiple pulses (likely representing separate LIPs), linked to the breakup of Rodinia and the consequent opening of the Iapetus Ocean. It is well represented in Laurentia [5–7] and Baltica [8–10], but also in other previously attached blocks, such as the Amazonian and West African cratons [11,12].

In the Pan-African Anti-Atlas Belt along the northern margin of the West African craton (WAC), the CIMP LIP is well represented by intrusives, volcanics, and sedimentary sequences forming the Ouarzazate Group ("PIII" or XIII of [13]; Figure 1). The latter was not deformed during the Pan-African Orogeny, suggesting its deposition in post-collisional setting during the extensional/transtensional stage in the Pan-African Belt [12,14–24]. The Ouarzazate Group covers a large area of ~2 × 10^6 km^2, with an estimated magma volume of ~1 × 10^6 km^3 and variable volcanic thickness between 300 and 2000 m, and resulted in intense hydrothermal activity, which produced diverse mineral deposits such as Imiter and Zgounder (Ag-Hg), Bou Azzer (Co-Ni-As-Ag-Au), Iourirn (Au), and Bou Madine (Cu-Pb-Zn-Au-Ag) [21,22,25,26].

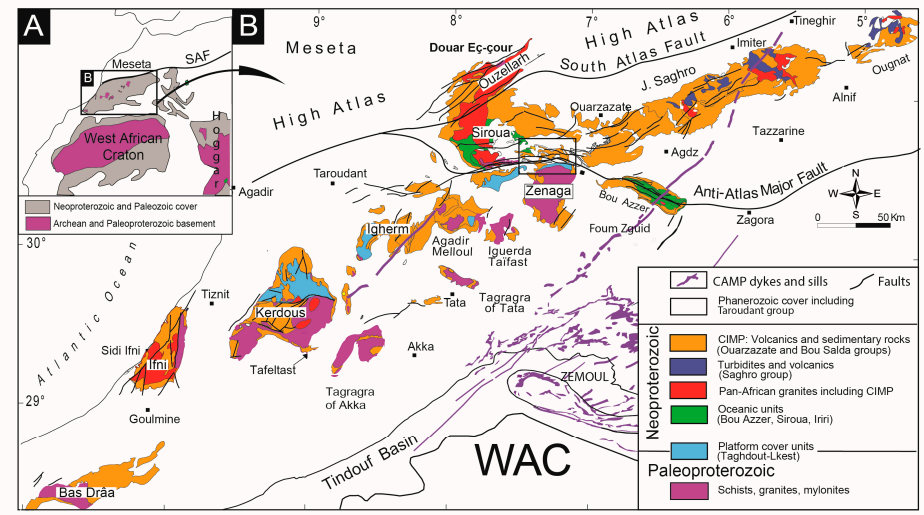

Figure 1. (**A)** The Anti-Atlas Belt at the northern margin of the West African Craton (WAC); (**B**) Geological map of the Anti-Atlas Belt in southern Morocco showing distribution of the OuarzazateGroup (i.e., the Central Iapetus Magmatic Province, CIM). Modified after [22,27]**.**

The most-complete and best-preserved volcanic sections of the Ouarzazate Group are in the Ouarzazate–Siroua–Bou Azzer regions, where the "locus typicus" of the Ouarzazate volcanic series was defined for the first time [13]. While the geochemistry, petrology, and U-Pb geochronology of the Ediacaran volcanic formations of the Anti-Atlas CIMP (i.e., Ouarzazate Group) have been extensively studied (e.g., [11,23,24,28–30] and references therein) some questions remain to be addressed. Furthermore, the geodynamic significance of the CIMP remains a topic of contention and a limited number of studies have been conducted on the physical characteristics of these volcanoes, facies architecture, emplacement mechanisms, eruption style, and facies model.

Among the post-collisional, Pan-African volcanic complexes of the Anti-Atlas (Morocco), the Taghdout Volcanic Field (TVF) of the Siroua Window (Central Anti-Atlas) (Figure 1), with its well-established Ediacaran age, is particularly interesting for its structural context, due to the vicinity of the Anti-Atlas Major Fault (AAMF), multiple volcanic facies, and eruptive dynamics and yet easy access. Volcanic eruptions predominantly took place in a continental environment during the Ediacaran period, between 580 and 545 Ma ([11,19,24,31–33], this work). These eruptions occurred following the last tectonic event of the Pan-African orogenic cycle (885–545 Ma), which was dated at ca. 608 ± 7 Ma in the Bou Azzer Inlier [24]. In addition, the main tectonic event (collision) of this orogenic cycle is dated at ca. 647 Ma in the Siroua Window [34].

In this paper, we will present new volcanological, petrographic, mineralogical, and geochemical data for the Ediacaran volcanic succession of the TVF in the Siroua Window of the Central Anti-Atlas, aiming to (i) describe the main lithofacies of the volcanic succession and propose a facies model for their emplacement, (ii) clarify their geochemical characteristics and magmatic affinities, (iii) discuss their petrogenesis and mantle sources, (iv) propose a geodynamic model for the Ediacaran Ouarzazate Group of Morocco. In addition, we will present a precise zircon U-Pb age for the top of the Ouarzazate volcanic pile and place it in the context of the available zircon U-Pb data for the Siroua Window and the rest of the Central Anti-Atlas.

2. Geological Background

The West-African Craton (WAC) is one of the five Precambrian cratons that form the African Plate, alongside the Kalahari, Congo, and Tanzania cratons and Sahara Metacraton. It contains two Archean basement shields; the Reguibat Shield in the north and the Leo-Man Shield in the south. Their Archean (3.5 to 2.7 Ga) cores, including greenstone belts and tonalite–trondhjemite–granodiorite (TTG) plutons, are surrounded by the Paleoproterozoic domains (2.35–2.00 Ga) and are covered by the Meso- to Neoproterozoic and younger sedimentary basins [35,36].

The Anti-Atlas Belt in southern Morocco, located along the northern margin of the West African Craton (WAC), forms a broad (800 km long and 200 km wide) anticlinorium with an ENE–WSW trend parallel to the Alpine High-Atlas Mountains. The belt is separated from the High-Atlas and Meseta domains by the South Atlas Fault in the north (SAF; Figure 1). The Precambrian basement is well exposed in several erosional inliers (known as "boutonnières"), within the late Ediacaran and younger rock units (Bas Drâa, Ifni, Kerdous, Tagragra of Akka, Tagragra of Tata, Igherm, Siroua, Zenaga, Bou Azzer, Saghro, and Ougnat; Figure 1), and aligned along two major fault systems, the South Atlas Fault (SAF) and the Anti-Atlas Major Fault (AAMF; Figure 1).

The Anti-Atlas Belt contains the Paleoproterozoic basement (affected by the Paleoproterozoic Eburnean Orogeny) unconformably overlain by the Anti-Atlas Supergroup (including the Lkest-Taghdout, Bou Azzer, Iriri, and Saghro groups sensu [28]), which is in turn unconformably overlain by the Ouarzazate Supergroup (related to the Pan-African Orogeny). The two major crust-forming periods of tectonothermal activity have been recognized during the Proterozoic in the Anti-Atlas Belt and are described below.

(i) The Paleoproterozoic Eburnean Orogeny (2.20–2.07 Ga). The Paleoproterozoic basement rocks outcrop exclusively SW of the AAMF [13], but they may also constitute the basement of the Pan-African Orogen to the NE [22,37,38]. They contain metasedimentary rocks, granites, paragneisses, and migmatites, with zircon U–Pb ages ranging from 2200 to 2030 Ma (e.g., [19,22,39–42]), intruded by dolerite dyke swarms with five clusters of ages: 2040, 1750, 1650, 1416–1380, and 885 Ma [43–46]. The ca. 2040 Ma felsic intrusive magmatism in the Anti-Atlas inliers is interpreted to be derived from melting of the lower crust via mafic underplating associated with the Tagragra of the Tata LIP [43]. The 885 Ma mafic magmatism is linked to Rodinia, and the 1750, 1650, and 1380–1416 Ma magmatic events are associated with the Nuna/Columbia extension (cf. [47,48]).

(ii) The Neoproterozoic Pan-African Orogeny (885–545 Ma). The Neoproterozoic sequences of the Anti-Atlas Belt associated with the Pan-African Orogeny are unconformably overlain by the post-collisional, volcano-sedimentary Ouarzazate Supergroup. The latter belongs to the Central Iapetus Magmatic Province (CIMP; [11,18,21,26,43,49,50]). The Neoproterozoic successions underlying the Ouarzazate Supergroup are subdivided into the lower units (Lkest-Taghdout, Bou Azzer, and Iriri groups), affected by all Pan-African orogenic events, and upper units (Saghro and Bou Salda groups), only affected by the latest stage of the Pan-African Orogeny (e.g., [21,22,28,40,43,51]).

The Lkest-Taghdout Group consists mainly of basalt, quartz sandstone, and stromatolitic/oolitic carbonate, intruded by dolerite dyke swarms and sill complexes [28,52]. Its lower and middle parts are Paleoproterozoic ([27,53] and references therein), while the upper part corresponds to the rifting at the northern portion of the WAC during the late Neoproterozoic at 885 Ma [27,54]. The rifting culminated with the opening of an oceanic basin on the northern margin of the WAC. The relics of the oceanic crust (Bou Azzer Group) are preserved in the Bou Azzer and Siroua inliers as strongly sheared, allochthonous ophiolite complexes ([23,55] and references therein). The ophiolitic assemblage mainly consists of ultramafic rocks (serpentinites with few chromite pods), but also includes mafic metacumulates, metabasaltic sheeted dykes, and pillow lavas [56–59]. Their geochemical signatures point to emplacement in a supra-subduction setting [59–66]. Zircon U–Pb dating of plagiogranite intrusions in the Siroua Inlier constrained oceanic accretion at ca. 760 Ma [59,67]. Subsequent to the opening of the ocean basin, subduction under an island arc was initiated (recorded by the Iriri Group in the Siroua Inlier; [19,68,69]). Migmatite from the Iriri Group yielded SHRIMP U–Pb ages at 743 ± 14 and 663 ± 13 Ma [19]. The older age refers to the emplacement of the migmatite protolith in an island–arc setting, whereas the younger age corresponds to ophiolite obduction and arc accretion followed by the regional metamorphism at the northern edge of the WAC in the Anti-Atlas Belt [19]. The development of the Anti-Atlas Belt oceanic arc complexes occurred during three magmatic flare-ups at ca. 750, 700, and 650 Ma that were punctuated by an early, major tectonic episode between 730 and 700 Ma [65,70]. A garnet Sm–Nd date of 647.2 ± 1.7 Ma was recently obtained for the regional metamorphism within the Tasriwine ophiolite complex of the Siroua Inlier [34]. This age is more than 15 million years younger than the previous age estimate [19]. North of the AAMF, in the eastern Anti-Atlas Belt (Figure 1), the oldest rocks are thick deposits of basalts and

turbidites of the Saghro Group, with detrital zircon U-Pb ages forming peaks at ca. 880 to 615 Ma [38]. The depositional age of and geodynamic constraints for the Saghro Group, unconformably overlying late Ediacaran Ouarzazate Group, are still debated and controversial [22,38,71–78]. Several authors suggested the Saghro Group was deposited in the early Neoproterozoic and age equivalent to the Tachdamt–Bleida passive continental margin sequence in the Bou Azzer Inlier [19,51,72,79–81]. Based on this interpretation, the age of the Saghro Group was considered to be Tonian to Cryogenian and its deformation has been linked to the main stage of the Pan-African Orogeny (650 Ma; [22,73,79]). Alternatively, it has been suggested that the Saghro Group was deposited in a back-arc setting [71,72,74,75,82] between the WAC margin and the northern Cadomian arc [29,76–78,83].

The post-collisional period (630–545 Ma) evolved from a transpressional to a transtensional tectonic setting, with the emplacement of large, high-potassium calc-alkaline to shoshonitic volcanic/plutonic bodies, accompanied by deposition of sedimentary successions in pull-apart basins and grabens. Deposition of the Bou Salda/Tidilline and Ouarzazate groups corresponds to the final stage of the Pan-African Orogeny. The Bou Salda/Tidilline groups (600–580 Ma) are characterized by poorly sorted sediments and diamictites associated with volcanic and intrusive rocks. The Bou Salda Group could be older than 600 Ma [19]. The Ouarzazate Group (580–545 Ma) is mainly composed of high-potassium, calc-alkaline volcanic, volcanoclastic, and plutonic rocks that are widely distributed in the High-Atlas and Meseta (e.g., [16,18,21,22,26,49,83–88]. The Ouarzazate Group was followed by deposition in the foreland basin represented by the Taroudant and Tata groups [49,84].

The Taghdout Volcanic Field (TVF, Siroua Window, Central Anti-Atlas) comprises volcano-sedimentary sequences represented by basalts, andesites, dacites, rhyolites, ignimbrites, conglomerates, sandstones, siltstones, and carbonates. They form volcanic successions that unconformably overlie the Neoproterozoic to Paleoproterozoic basement in the Aguerzoula, Taghdout, and Tinzaline subinliers, located to the north of the MAAF. This defines the northern border of the Zenaga Inlier and the margin of the WAC (Figure 2). The TVF, 26 km long and 8 to 10 km wide, forms a NW–SE arc, with dips around 20° towards the north or northeast; it is displaced by multiple strike–slip faults, running NE–SW to E–W.

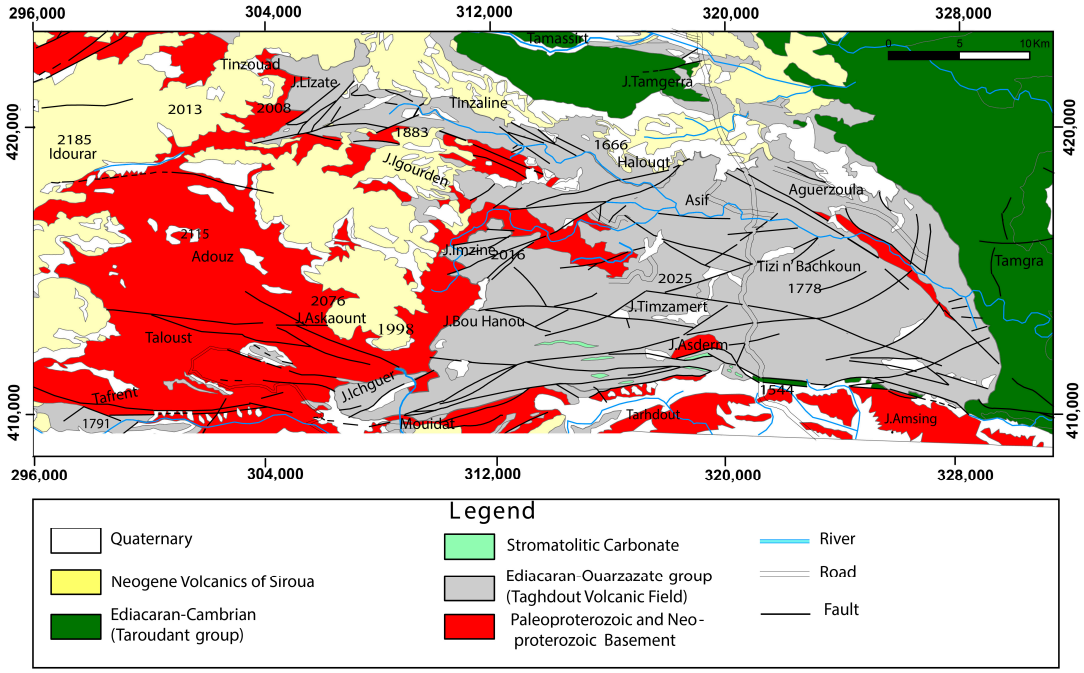

Figure 2. Geological map of the Taghdout Volcanic Field, TVF (Siroua Window, Central Anti-Atlas, Morocco). Modified from [13].

3. Materials and Methods

3.1. Stratigraphy and Petrography of Volcanic Sequences

This study is the result of extensive fieldwork on the Taghdout Volcanic Field (TVF), including the study of outcrops and the stratigraphic logging of eight sections. We have produced a comprehensive volcanic stratigraphy of the area, identifying the products of each individual eruption, their relative stratigraphy, and surface area. Volcanic stratigraphy is an essential tool for understanding the evolution and volcanic history of this volcanic field and for establishing a correct facies model for its emplacement and architecture. Petrographic analysis was carried out on a total of 200 thin sections, allowing the study of textures and mineralogical composition.

3.2. High-Precision U-Pb Geochronology Employing CA-ID-TIMS Technique

Selected zircons from sample SI88 were analyzed for high-precision geochronology using chemical abrasion, isotope dilution, thermal ionization mass spectrometry (CA-ID-TIMS) at ETH Zurich. The crystals were annealed at 900 °C for over 60 h and subsequently loaded in Teflon microcapsules for chemical abrasion with concentrated HF and placed in a high-pressure Parr bomb at 190 °C for 12 h. Afterwards, the zircons were transferred to Teflon beakers and washed in 6N HCl on a hot plate (at 80 °C) and in 4N HNO_3 in an ultrasonic bath. The crystals were then loaded back into the pre-cleaned microcapsules for dissolution with concentrated HF and trace HNO_3. The EARTHTIME ^{202}Pb-^{205}Pb-^{233}U-^{235}U isotope tracer solution (ET2535; [89,90]) was added to ensure complete sample–spike equilibration. The zircons were dissolved in Parr bombs over 60 h at 220 °C.

The solutions were subsequently dried down and redissolved in 6 N HCl at 190 °C for 4–6 h in the Parr bombs. Then, the solutions were dried down and redissolved in 3N HCl for column chemistry, modified after [91], which efficiently separates Pb and U from other elements. Uranium and Pb were collected and dried down with one drop of 0.02 M H_3PO_4. Finally, the samples were loaded onto outgassed, zone-refined Re filaments with a silica gel emitter (modified after [92]).

Analyses were conducted on a Thermo TRITON Plus thermal ionization mass spectrometer equipped with an axial secondary electron multiplier and Faraday cups connected to 1013 Ω amplifiers in a setup described in [93,94]. Lead and U isotopes were analyzed using static multicollection in the Faraday cups, except for ^{204}Pb, which was analyzed in the axial secondary electron multiplier. Pb and U mass fractionations were corrected using the double spike (ET2535) and assuming a sample $^{238}U/^{235}U$ ratio of 137.818 ± 0.045 (2σ; [95]). Data reduction and visualization were performed using Tripoli and UPb Redux software (v. 3.7.1) [96]. $^{206}Pb/^{238}U$ dates were corrected for initial $^{230}Th/^{238}U$ disequilibrium using a constant Th-U partition coefficient ratio of 0.2. All dates are reported with 2-sigma uncertainty which are presented as μ ± x|y|z, where μ is the date, x is the uncertainty including only analytical uncertainties, y includes the uncertainty of the tracer calibration, and z also includes the uncertainty on the decay constant.

3.3. Electron Microprobe Analyses

Electron microprobe (EMP) analyses of clinopyroxene were carried out with a CAMEBAX microprobe (Camparis, University Pierre and Marie-Curie of Paris VI, Paris, France) using oxide standards and natural minerals for calibration. Operating conditions included an acceleration voltage of 15 kV, a beam current of 40 nA, a minimum beam

diameter of 1 μm, and a counting time varying between 10 and 40 s, depending on the element. The analytical accuracy and precision estimated from repeated analyses on natural standards are within ±2% for major elements and ±5% for minor elements. The units of the clinopyroxene formula have been calculated on the basis of 6 oxygen atoms.

3.4. Whole Rock Geochemistry

To investigate the tectonic setting of the Taghdout Volcanic Field (TVF), we combined our own geochemical data [14,97] and previously published literature data [98,99].

Element concentrations for whole rock analyses were determined at the "Service d'Analyse des Roches et des Minéraux" of the Geochemical and Petrographic Research Centre in Nancy (SARM Laboratory-CRPG-CNRS, Nancy, France). To avoid contamination, crushing and pulverization were carried out using agate mills. Powders were treated with $LiBO_2$, dissolved with HNO_3, and analyzed and calibrated with international geostandards (basalt BE-N, basalt BR, dolerite WS-E, and microgabbro PMS). Major and trace elements were analyzed by inductivelycoupled plasma–atomic emission spectroscopy (ICP-AES) and inductivelycoupled plasma–massspectrometry (ICP-MS), respectively. The analytical procedures are described in detail at https://sarm.cnrs.fr/index.html/ (URL accessed on 28 January 2025). The asterisk-marked rocks were also analyzed for REE and additional trace elements by the neutron activation method. The method used was pure instrumental activation analysis (without chemical separation) using epithermal neutron irradiation (OSIRIS reactor at Saclay, France, "Commissariat de l'Enérgie Atomique, Groupe des Sciences de la Terre, Laboratoire Pierre Süe"). Irradiation was carried out in Cd vials, followed by several measurements taken at different intervals from 8 days to 1 month after irradiation [100]. The reference standard used was GNS [101], while the sample standard used was BEN [102].

4. Results

4.1. Fieldwork Observations, Volcanic Stratigraphy, and Petrography

4.1.1. The Volcanic Succession of the Jbel Adrar Tougmast Type Section

The detailed distribution of facies both laterally and vertically was examined and is illustrated in Figure 3. Depending on the area, a thickness between 420 and almost 1500 m of effusive, pyroclastic, and siliciclastic rocks was deposited, representing between 480 and 600 km^3 of volcanic and sedimentary deposits. Accumulation of these volcano-sedimentary sequences is the result of a volcanic evolution that differed in time and space. The most complete volcanic successions are exposed at Adrar Tougmast, Bou Hanou, South Aguerzoula, and North Aguerzoula (Figure 3, columns A, B, F, and H)

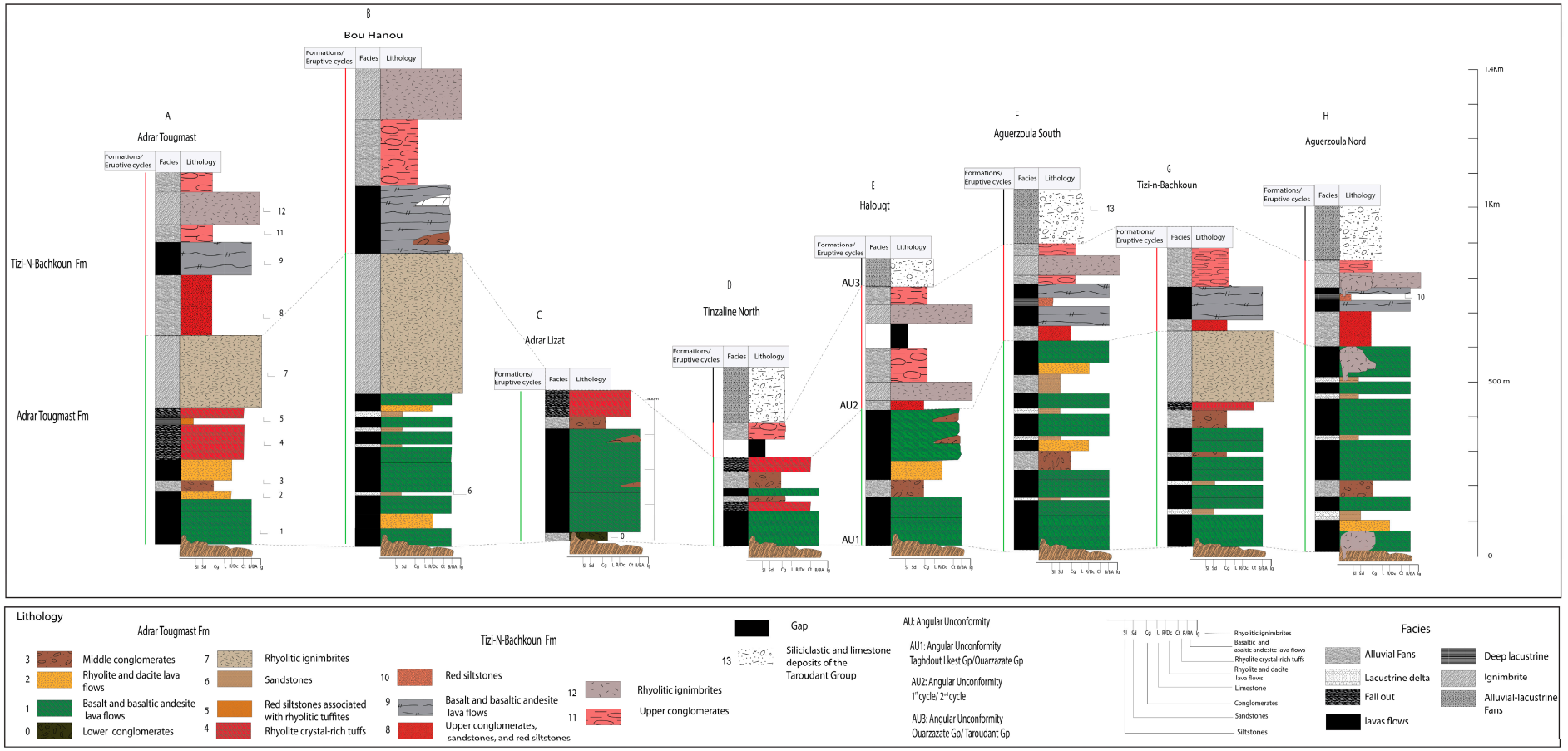

Figure 3. Lithostratigraphic columns across the Ediacaran Taghdout Volcanic Field (TVF), modified after [14]. Legend: 0—Lower conglomerates; 1—Basalt, andesite, and hybrid lava flows and associated pyroclastic rocks (flow breccias and/or blast breccias); 2—Rhyolite and dacite lava flows; 3—Middle conglomerates; 4—Rhyolite crystal-rich tuffs; 5—Red siltstones associated with rhyolitic tuffites; 6—Sandstones; 7—Rhyolitic ignimbrites; 8—Upper conglomerates, sandstones, and red siltstones; 9—Basalt and basaltic andesite lava flows; 10—Red siltstones; 11—Upper conglomerates; 12—Rhyolitic ignimbrites associated with rhyolitic domes and lava flows; 13—Siliciclastic and limestone deposits of the Taroudant Group. Abbreviations: Fm—Formation.

The Jbel Adrar Tougmast lithostratigraphic column (Figure 3, column A) was measured in the section at the base of Jbel Adrar Tougmast. It represents a succession of lithofacies that are separated by an angular unconformity into two main formations: the Adrar Tougmast Formation at the base, overlain by the Tizi-n-Bachkoun Formation (Figure 4A).

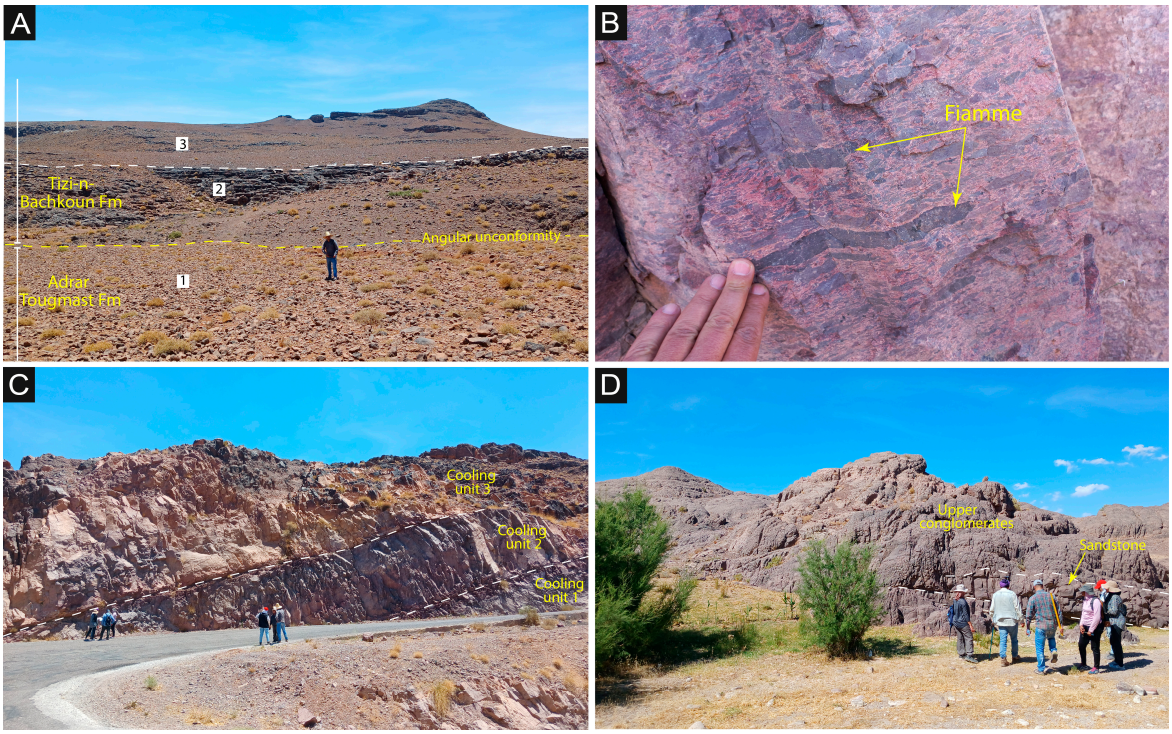

Figure 4. Field photos of the Taghdout Volcanic Field in the Siroua Window. (**A**) Panoramic view in the Tizi-n-Bachkoun Pass section, showing the angular unconformity between the Adrar Tougmast Formation (rhyolitic crystal-rich tuffs) (1) and the Tizi-n-Bachkoun Formation (basalt and basaltic andesite flows) (2); the ridge comprises red siltstones and upper conglomerates (3). (**B**) rhyolitic ignimbrites with fiamme of the Tizi-n-Bachkoun Pass section; (**C**) panoramic view of a sequence of ignimbrites with fiamme of the Adrar Tougmast Formation. At least three cooling units can be seen on the photo; (**D**) upper conglomerates at the top of the Tizi-n-Bachkoun Formation. Abbreviations: Fm—Formation.

The Adrar Tougmast Formation

The formation consists of the following sequences described in ascending order: (i) A 140 m thick sequence of basalt, andesite, and hybrid lava flows and associated volcaniclastic facies that unconformably overlies the Paleoproterozoic basement with quartz sandstones of the Taghdout-Lkest Group. It begins with about 40 m of porphyritic andesites with plagioclase megacrysts. In the thin sections, porphyritic andesites have large euhedral phenocrysts of mostly plagioclase and less commonly hornblende and pyroxene. Less common are phenocrysts of biotite, apatite, ilmenite, magnetite, and titanomagnetite (Figure 5A)

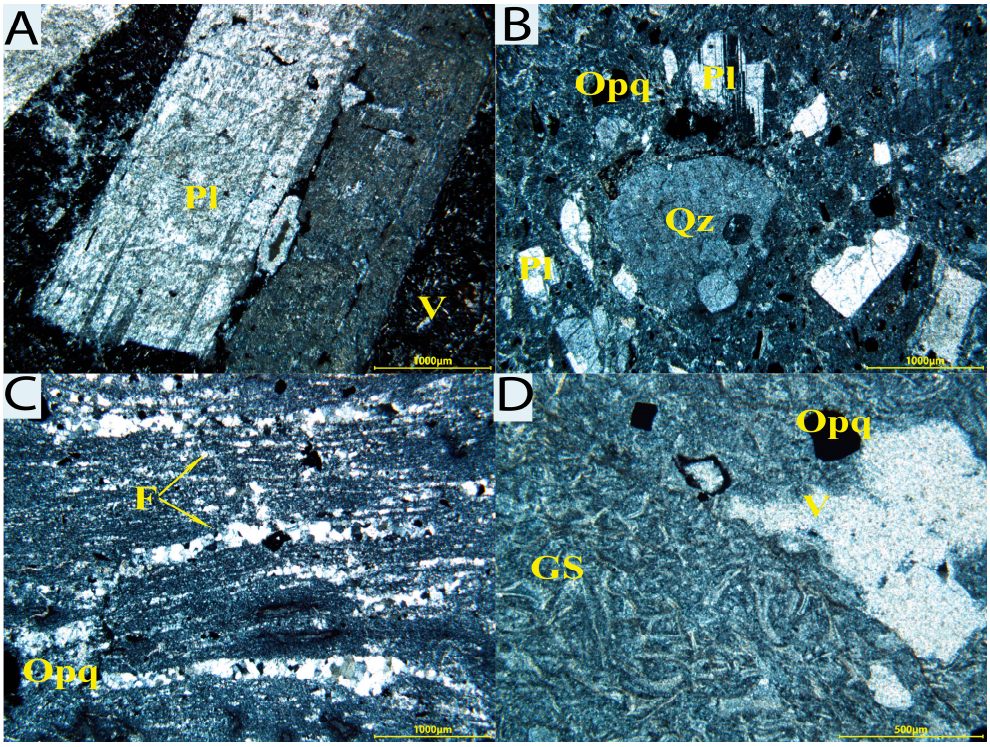

Figure 5. Thin-section photomicrographs showing textures of volcanic rocks of the Taghdout Volcanic Field of the Sirwa Window: (**A**) Porphyritic andesite with megacrysts of plagioclase. The groundmass consists mainly of plagioclase microliths and minor vesicles, sample NS1; (**B**) crystalrich quartz, with plagioclase, moderately welded ash flow tuff with the groundmass consisting of quartz, alkali feldspar, and oxide mineral, sample TZ110; (**C**) ignimbrites with fiamme, sample HQ-138; (**D**) vitroclastic texture with glass shards, sample H114. Abbreviations: F = fiamme, GS = glass shards, Opq = oxide mineral, Pl = plagioclase, Qz = quartz, V = vesicle. Figure 5A,B,D are cross-polarized light images, whereas Figure 5C is a plane-polarized light image.

(ii) A 110 m thick sequence of porphyritic rhyolite and dacite lava flows separated by a lenticular conglomerate (middle conglomerate). The porphyritic rhyolite consists of quartz, oligoclase, sanidine, and, less commonly, amphibole, biotite, and pyroxene phenocrysts in a fine-grained matrix of mainly quartz and feldspar. The porphyritic dacite shows quartz vein stockwork.

(iii) A 140 m thick succession of crystal-rich, quartz- and biotite-bearing, moderately welded ash flow tuff. The phenocryst content is >30%, typically of feldspar, quartz, and biotite, with a few percent of porphyritic, juvenile fragments and aphanitic, volcanic lithic fragments. Locally, the eutaxitic texture is well developed in this unit (Figure 5B). An interval of red siltstones occurs near the top of the sequence, indicating a volcanic quiescence.

(iv) A 200 m thick sequence of welded, rhyolitic ignimbrite with fiammes and scattered lithic fragments (Figures 4B and 5C). At least three cooling units can be distinguished (Figure 4C,D).

Tizi-n-Bachkoun Formation

Above the angular unconformity, the Tizi-n-Bachkoun Formation is composed of:

(v) A 200 m thick, siliciclastic fluvial sequence of conglomerates, sandstones, and siltstones (upper conglomerates).

(vi) A 100 m thick sequence of basalt and basaltic andesite lava flows (Figure 4A).

(vii) Fifty-meter-thick conglomerates that comprise poorly sorted boulder beds, horizontally stratified pebbly to blocky to clast-supported beds, and lenticular sandstones.

Boulders are subrounded to subangular and are occasionally imbricated. Oversized boulders (up to 160 cm) of lava flow and ignimbrite are occasionally present.

(viii) One-hundred-meter-thick eutaxitic ignimbrites, typically with fiammes and glass shards (Figure 5D), and matrix-supported lapilli tuffs with vitroclastic matrix. Some lapilli tuffs lack matrix and show mostly unfractured crystals but contain oriented, devitrified fiamme. These textural features suggest rheomorphic ignimbrites. Locally, ignimbrites are associated with rhyolitic domes and lava flows.

(ix) Ninety-meter-thick fluvial conglomerates (upper conglomerates).

4.1.2. Stratigraphic Correlation with Other Regions

The lithostratigraphic columns established for other areas show significant differences relative to the Jbel Adrar Tougmast section, indicating lateral variations within the volcanic succession.

(i) In the Bou Hanou area (Figure 3, column B), there is an increase in the thickness of the volcanic pile compared to the Jbel Adrar Tougmast section due to the multiple basaltic and andesitic lava flows with sandstone intercalations and a thicker sequence of rhyolitic ignimbrites with up to six cooling units. Furthermore, the siliciclastic sedimentary sequence that precedes deposition of the basalt and basaltic andesite flows of the Tizi-n-Bachkoun Formation is absent there. Instead, lenticular conglomerate layers and lacustrine, stromatolitic limestones characterize the latter formation in this area.

(ii) In the Lizate area, volcanic pile is up to 435 m (Figure 3, column C) with a decametric interval (maximum thickness of 50 m) of polymictic conglomerates (lower conglomerates) having quartzite, schist, and granite pebbles at the base of the volcanic pile. The porphyritic rhyolite and dacite lava flows and the welded rhyolitic ignimbrite with fiammes of the Adrar Tougmast Formation are also absent. Further, the upper sequence of the volcanic succession (the Tizi-n-Bachkoun Formation) is missing there, suggesting a topographic high (uplift) in this area during the emplacement of the units of the second eruptive cycle.

(iii) In the Tinzaline area (Figure 3, column D), the volcanic pile thickness is reduced compared to the Jbel Adrar Tougmast section and most of the upper units of the Tizi-n-Bachkoun Formation are absent.

(iv) In the Halouqt area (Figure 3, column E), the rhyolitic, crystal-rich tuff sequence of the Adrar Tougmast Formation and basaltic and basaltic andesite lava flows of the Tizi-n-Bachkoun Formation are missing.

(v) In the Aguerzoula Inlier (Figure 3, columns F, G, and H), the rhyolitic, crystal-rich tuff sequence (Figure 3, columns F and H) and dacite lava flows (Figure 3, column G) are absent. Hybrid lavas are generally abundant. In Tizi-n-Bachkoun, the sequence of crystal-rich tuffs and ignimbrites is well exposed with several cooling units. The basaltic and basaltic andesite lava flows of the Tizi-n-Bachkoun Formation often show intercalations of red siltstones. The rhyolitic bodies often form domes in association with ignimbrites, having small thickness and short lateral extent.

4.2. CA-TIMS Zircon U-Pb Geochronology

We analyzed a total of six single zircon crystals from sample SI88. Five out of six zircons yielded indistinguishable 230Th-corrected $^{206}Pb/^{238}U$ dates with a weighted mean of 557.613 ± 0.043 Ma (MSWD = 0.33; see Supplementary Material Table S1). One zircon yielded a younger date of ca. 556 Ma (Figure 6) that we consider reflecting residual Pb loss. The weighted mean $^{206}Pb/^{238}U$ date of SI88 tightly constrains the age of the upper part of the volcanic pile and together with previous ages constrains the duration of volcanic activity in the Taghdout Volcanic Field and the Ouarzazat Group as a whole (see Section 5.3).

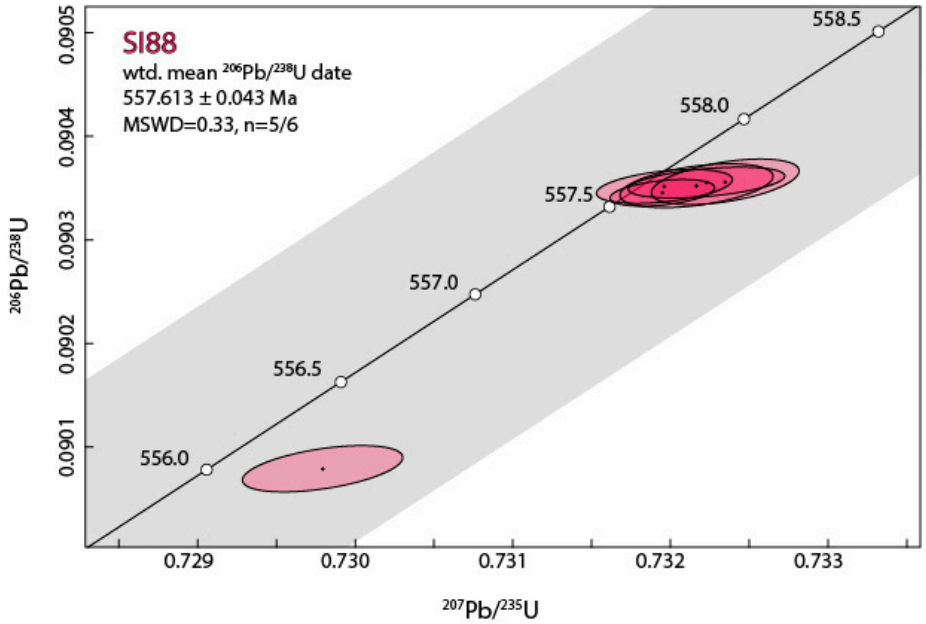

Figure 6. CA-ID-TIMS zircon U–Pb geochronology for sample SI88 of the Taghdout Volcanic Field.

4.3. Whole-Rock Geochemistry

The representative whole-rock major and trace element data (REE included) of the Ediacaran TVF volcanics are presented in the Supplementary Materials (Table S2). The used geochemical database is compiled from both the literature data [14,97–99] and new data presented herein.

The lithostratigraphic data for the Ediacaran TVF allow for distinguishing the Adrar Tougmast and the Tizi-n-Bachkoun formations, separated by an angular unconformity and characterized by very different volcanic facies. This was taken into account to group the studied volcanic rocks (including pyroclastics) into two main cycles: (i) the first cycle (1st cycle) corresponds to the Adrar Tougmast Formation that forms the lower part of the TVF volcanic pile and that includes lavas of basaltic to rhyolitic compositions, but also hybrid lava flows and ignimbrites, and (ii) an upper sequence (2nd cycle) corresponding to the Tizi-n-Bachkoun Formation, also composed of basaltic to rhyolitic lavas rocks and including breccia and ignimbrites.

4.3.1. Classification of Volcanic Rocks of the Ediacaran Taghdout Volcanic Field

Since the studied rocks show evidence of greenschist-facies metamorphism (association of albite, actinolite, and chlorite) and because high-field strength elements like Nb and Y are less susceptible to alteration during metamorphism than Na_2O and K_2O, we used the SiO_2-Nb/Y diagram [103], considered to be more reliable to distinguish the geochemical affinities of altered rocks than alkali-based schemes. On such a diagram (Figure 7), the volcanic rocks of both eruptive Ediacaran TVF cycles are plotted in the subalkaline
field ranging in composition from basalts to rhyolites (SiO_2 = 44.6 to 80.8 wt%). According to the systematics shown in Figure 7, the compositional range of the 1st cycle comprises basalts, andesites, rhyodacites/dacites, and rhyolites, while the 2nd cycle ranges in composition from basalts to rhyolites through basaltic andesites. In order to facilitate rock description, they were arbitrarily subdivided into “mafic” and “felsic” rocks, these terms being used in a sensu lato. The mafic group includes basalts and andesites whereas the felsic group includes rhyodacites, dacites, and rhyolites.

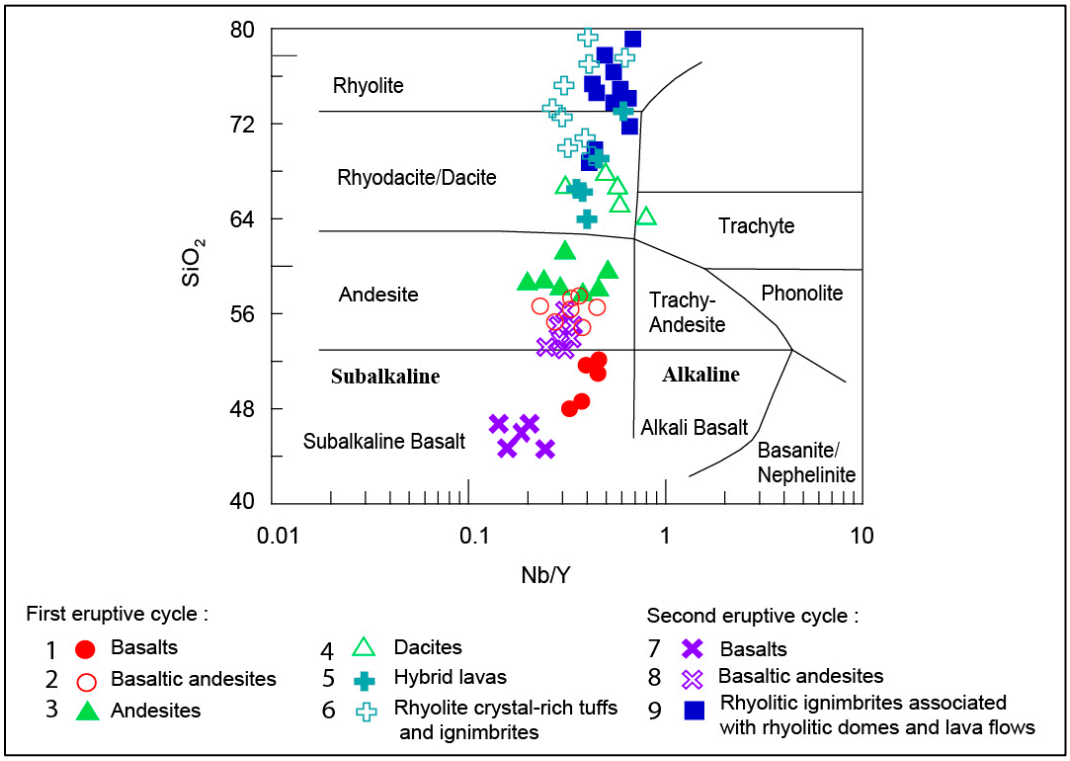

Figure 7. Plot of the studied rocks on the SiO2 vs. Nb/Y diagram [103].

4.3.2. Geochemistry of Volcanic Rocks of the 1st Cycle of the Taghdout Volcanic Field

The volcanic rocks of the first eruptive cycle of the TVF (i.e., the Adrar Tougmast Formation) range in SiO_2 content from 47.7 to 80.8 wt.%, from mafic to felsic compositions.

Mafic Rocks

The mafic rocks of the 1st eruptive cycle of the TVF range in SiO_2 content from 47.7 to 57.5 wt.% and have Mg# values (Mg# = $Mg^{2+}/(Mg^{2+} + Fe^{2+})$ from 0.10 to 0.61, with correspondingly variable transition element contents (Ni = 8–68 ppm, Cr = 5–188 ppm, Co 16–54.4 ppm, Sc = 20.7–30.4 ppm). In agreement with their subalkaline characteristics, TiO_2 contents are low, from 0.98 to 2.30 wt%.

Primitive mantle-normalized trace element "spidergrams" for the mafic rocks of the 1st eruptive cycle of the TVF (Figure 8) are characterized by variable fractionation of REE, with enrichments of more incompatible LREE over HREE, corresponding to $(La/Yb)_N$ = 1.53–8.37 (Figure 8A). They are characterized by significant negative anomalies of Nb ($(Th/Nb)_N$ = up to 8.39), Ta, and Sr and less pronounced Ti anomaly (Figure 8B).

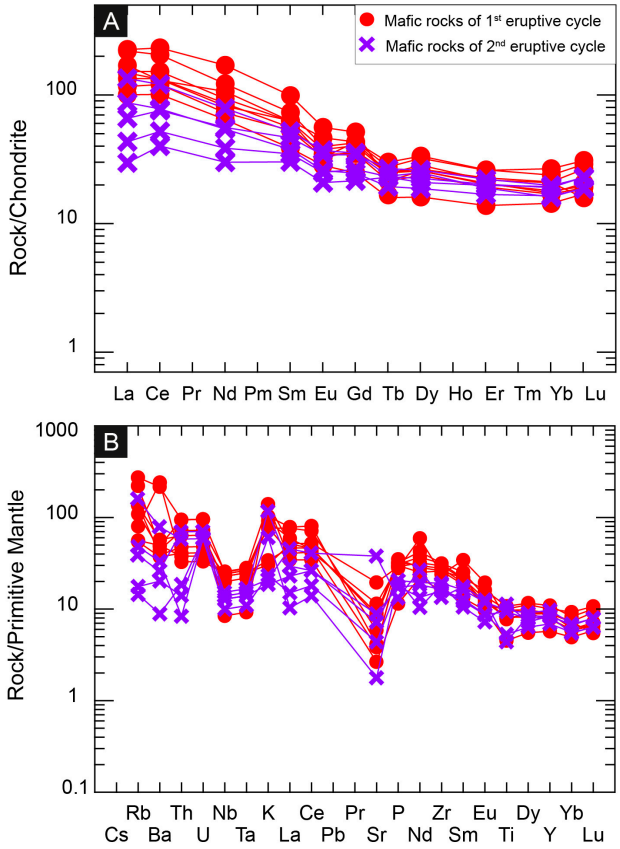

Figure 8. (**A**) Masuda–Coryell-type Rare Earth Element diagram [104] for the analyzed mafic rocks of the TVF of the Siroua Window. Only non-cumulate rocks are plotted. C1 chondrite values for normalization are from [105]. (**B**) Primitive mantle-normalized trace element "spidergram" for the analyzed mafic rocks of the TVF of the Siroua Window. Primitive mantle values for normalization are from [105].

Felsic Rocks

The herein considered felsic rocks of the 1st eruptive cycle of the TVF are characterized by SiO_2 contents varying from 57.58 to 80.80 wt%, with Mg# values ranging from 2.24 to 43.10 and TiO_2 contents from 0.71 to 1.64 wt%. They have largely peraluminous to slightly metaluminous, high-K calc-alkaline to calc-alkaline compositions (Figure 9A,B). Their REE patterns are characterized by significantly more pronounced Eu negative anomalies (Eu/Eu* = down to 0.12) compared with the mafic rocks from the same cycle (Eu/Eu * = 0.75 to 0.95).

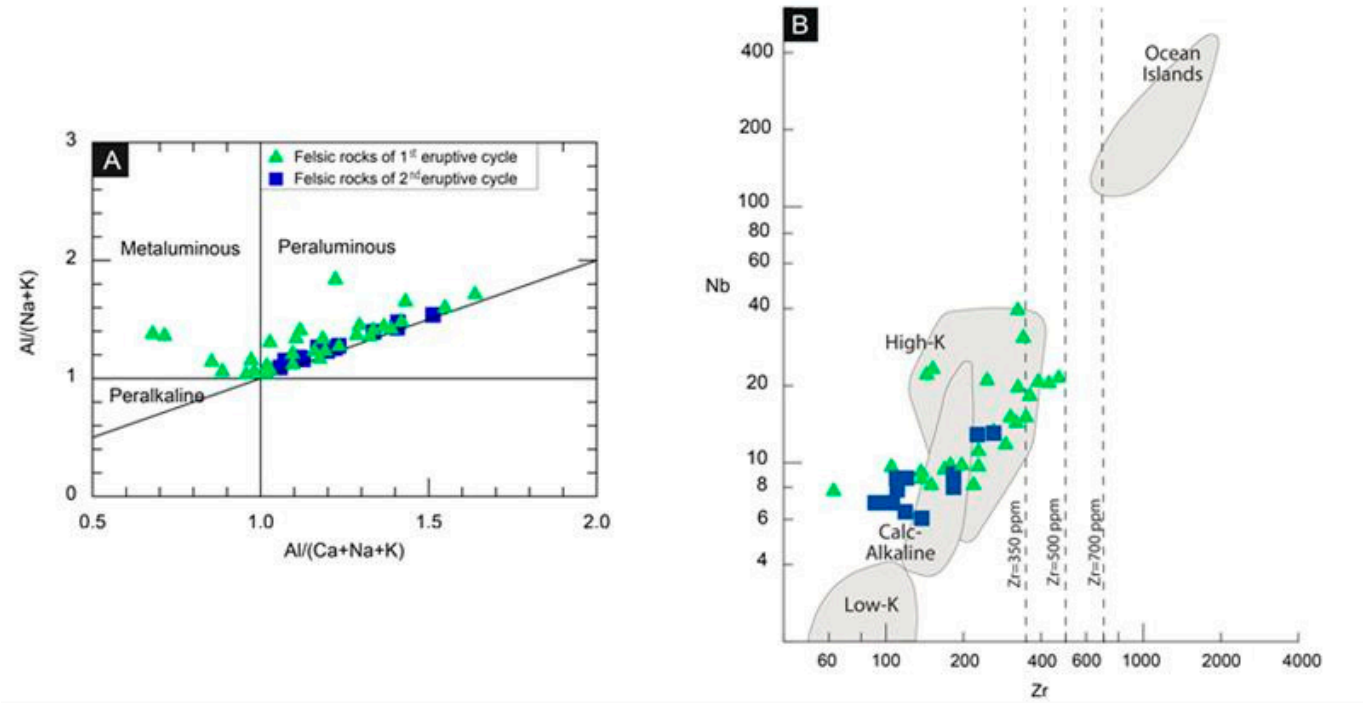

Figure 9. (**A**) Aluminum saturation diagram after [106,107]. (**B**) Geochemical characterization of the felsic volcanic and pyroclastic rocks of the TVF in the Nb-Zr diagram of [108].

The felsic rocks, plotted in the normalized multielement diagrams ("spider diagrams"), correspond to different stages of magma evolution, with almost all of them showing similar primitive-mantle-normalized patterns (Figure 10A,B), potentially indicating comagmatism. The patterns are all characterized by a significant enrichment in LILE (Rb, Ba, K, and Th), significant and systematic Sr and Ti negative anomalies, with most of them also having marked Nb and Ta negative anomaly ($(Th/Ta)_N$ = up to 4.14; $(Th/Nb)_N$ = up to 9.44).

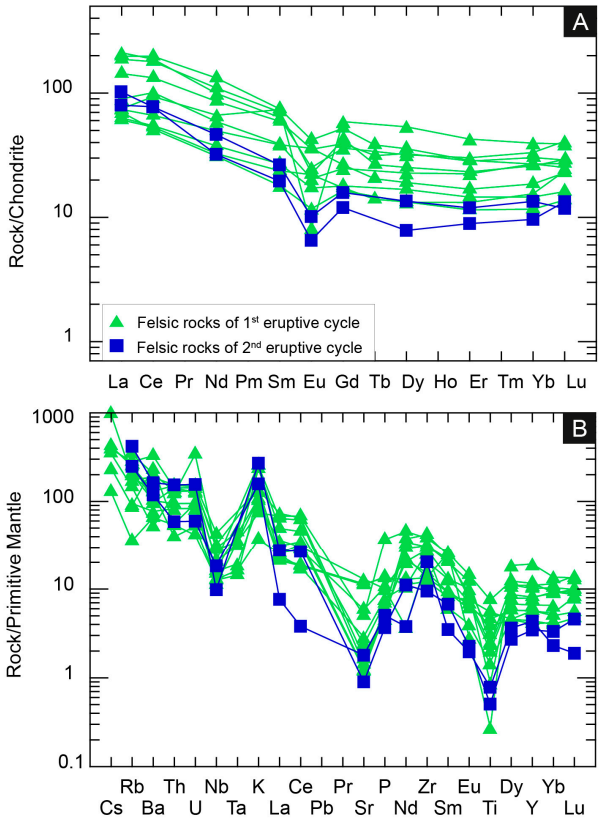

Figure 10. (A) Masuda–Coryell-type Rare Earth Element diagram [104] for felsic rocks of the TVF of the Siroua Window. Chondrite values for normalization are from [105]. (**B**) Primitive-mantle-normalized trace element "spidergram" for felsic rocks for the TVF of the Siroua Window. Primitive mantle values for normalization are from [105].

4.3.3. Geochemistry of Volcanic Rocks of the 2nd Eruptive Cycle of the TVF

The volcanic rocks of the 2nd eruptive cycle of TVF (the Tizi-n-Bachkoun Formation) range in SiO_2 content from 44.6 to 79.2 wt%, corresponding to ultramafic to felsic composition. This cycle, in contrast to the first one, is clearly bimodal with a significant gap in silica content between 56.2 and 68.9 wt%.

Mafic Rocks

Mafic rocks of the 2nd eruptive cycle of the TVF are characterized by SiO_2 content ranging from 44.6 to 55.0 wt%and have Mg# varying from 0.22 to 0.50 and variable transition element content (Ni = 13–181 ppm, Cr = 17–311 ppm, Co 12–66 ppm, Sc = 25.9–37.5 ppm). TiO_2 contents are low, 0.96 to 2.41 wt%.

When compared with the mafic rocks of the 1st cycle, the mafic lithologies of the Tizi-n-Bachkoun Formation are significantly less enriched in incompatible elements, as shown, for example, by La (6.98 to 31.6 ppm vs. 21 to 56.15 ppm for the 1st cycle), and have less fractionated REE patterns ($(La/Yb)_N$ = up to 8.37) compared to the 1st cycle (up to 13.15). In the normalized multielement diagrams ("spider diagrams"), basalt patterns for the second eruptive cycle of the TVF (Figure 8A) are more variable in LILE (Ba, U, Th) concentrations, having strong Nb, Sr, and Ta negative anomalies (e.g., $(Th/Nb)_N$ = 3.50–5.25).

Felsic Rocks

Felsic rocks of the 2nd eruptive cycle of the TVF have peraluminous, calc-alkaline to high-K calc-alkaline compositions (Figure 9A,B). They show significantly fractionated LREE compared to HREE ($(La/Yb)_N$ = 3.13–12.16; 7.03 on average) and systematic negative anomalies in Eu (Figure 10A). In the normalized multielement diagrams ("spider diagrams"), rhyolites of the 2nd eruptive cycle of the TVF display uniform patterns (normalized to the primitive mantle, [105]; Figure 10B). The patterns are characterized by a significant enrichment in LILE (Rb, Ba, K, and Th) and pronounced negative anomalies in Nb and Ta (normalized Th/Ta ratio varies from 5.07 to 8.58 with an average of 6.83 and normalized Th/Nb ranges from 3.23 to 15.98 with an average of 10.69). Systematic negative anomalies are also observed for Ti.

4.4. Mineral Chemistry of Clinopyroxene

Clinopyroxene (cpx) in the studied rocks occurs as either a matrix component or as phenocrysts but is rarely well preserved. In most cases, clinopyroxene is entirely replaced by calcite, epidote, iron oxides, and chlorite, forming ghosts only recognizable by their habit.

Two representative samples from the basaltic andesite of the Adrar Tougmast Formation (Sample YS 60) and basalt of the Tizi-n-Bachkoun Formation (Sample YS 22) were selected for pyroxene composition analyses (Supplementary Materials Table S3).

The clinopyroxenes of the basaltic andesites of the Adrar Tougmast Formation (1st cycle) are augite with an average value of En43-Wo42-Fs15 (Figure 11A). Their chemical characteristics indicate that they are pyroxenes typical of non-alkaline basalts: having high silica content (51.48 wt% ≤ SiO_2 ≤ 53.53 wt%) with relatively low alumina (1.62 wt% ≤ Al_2O_3 ≤ 3.29 wt%, with an average of 2.23 wt%) and titanium (0.40 wt% ≤ TiO_2 ≤ 0.78 wt%with an average of 0.54 wt%) contents and low alkaline and alkaline earth contents ([Ca + Na] < 1) (Figure 11B). The clinopyroxenes of the Tizi-n-Bachkoun Formation (2nd cycle) basalts are also augites with an average value of En42-Wo40-Fs18 (Figure 11A), showing identical non-alkaline chemical characteristics: high silica content (48.87 wt% ≤ SiO_2 ≤ 53.62 wt%), low titanium (0.45 wt% ≤ TiO_2 ≤ 1.03 wt%, with an average of 0.78%), aluminum (1.38 wt% ≤ Al_2O_3 ≤ 3.43 wt% with an average of 2.58 wt%), and alkaline and alkaline earths ([Ca + Na] < 1) concentrations. The calc-alkaline nature of the magmas from which the clinopyroxenes crystallized is indicated in Figure 11C.

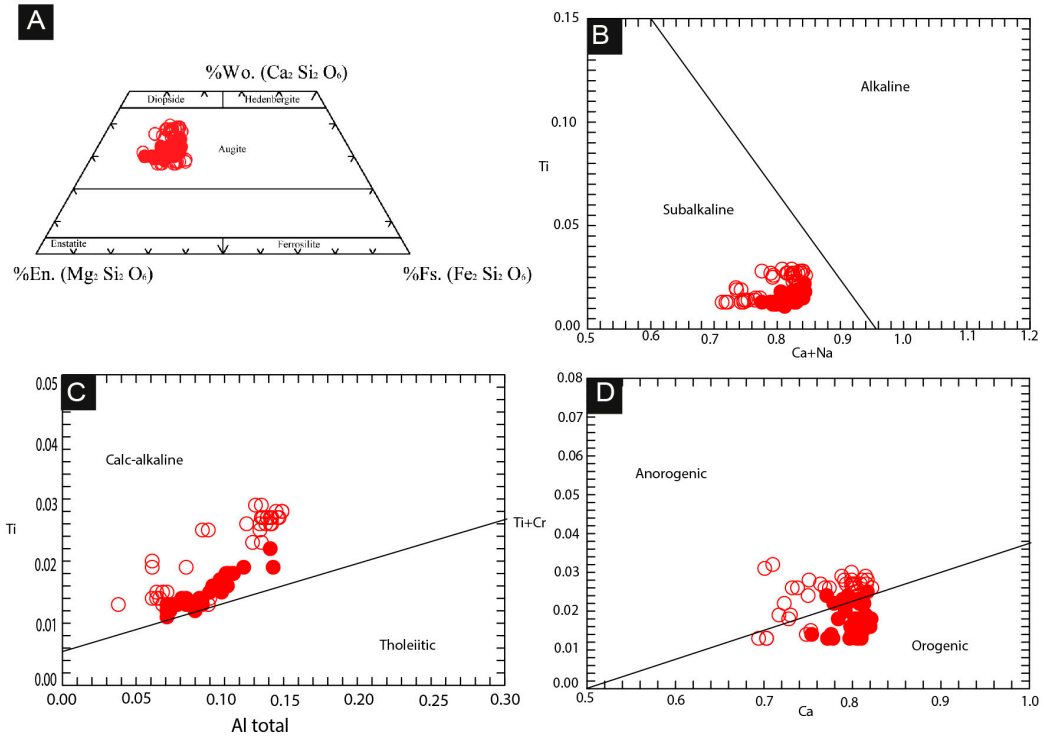

Figure 11. (**A**) Composition of the clinopyroxenes from basaltic andesites of the 1st eruptive cycle of Taghdout Volcanic Field (Adrar Tougmast Formation; solid circles) and basalts of the 2nd eruptive cycle of the Taghdout Volcanic Field (Tizi-n-Bachkoun Formation; empty circles) in the enstatite (En), wollastonite (Wo), and ferrosilite (Fs) triangle [109]. (**B**–**D**) Composition of the studied clinopyroxenes in three discriminant diagrams [110].

5. Discussion

5.1. Depositional Environment of the Ediacaran Volcanism of the TVF

Geological and paleogeographic frameworks of the region during the Ediacaran period (intracontinental basin developed during the gravitational collapse of the Pan-African Orogen), lithofacies (a'a lava flows and lacustrine and fluvial deposits), the large volume of outcropping materials (480 km^3 to 600 km^3), and short duration of volcanic eruptions (9 Ma minimum to 23 Ma maximum) clearly point to a large igneous province (LIP) emplaced in a continental setting. Characteristics of the lava flows indicate predominantly subaerial eruption (e.g., a'a lava). Pyroclastic rocks contain juvenile, pyroclastic fragments with significant vesiculation (50 to 80% vesicles by volume which may suggest strombolian eruptions).Conglomerates and domal and crinkly laminated stromatolites are interbedded in the volcanic succession. These lithologies carry sedimentological features, indicating continental, fluvial, and lacustrine sedimentary environments.

5.2. Facies Analysis of the TVF

The goal of facies analysis is to reconstruct spatial and temporal variations in the geometry of volcanic, volcaniclastic, and sedimentary facies associations. It results in stratigraphic reconstructions, characterizing the volcanic succession over the entire volcanic region. This approach, developed by [111], aims to define on a regional scale a framework of volcanic processes at the surface, over a given eruptive cycle, in a given continental and/or marine environment, depending on the nature and type of the erupted products (e.g., mafic vs. felsic; lava flows, domes, pyroclastites), the relative volume and their spatial distribution, and the stratigraphic and lateral relative abundance of

sedimentation style (e.g., fluvial, lacustrine, marine, etc.). Establishing a volcanic facies model based on this analysis allows comparison with other examples and integration into a geodynamic context of the studied volcanism.

During the 1st eruptive cycle, the Ediacaran volcanism of the TVF had the following volcanological characteristics: (1) eruptions occurred in a subaerial continental environment; (2) stratigraphic and lateral facies variations were abrupt; (3) non-bimodal volcanism was characterized by volumetric predominance of rhyolitic and andesitic magmas over basaltic, dacitic, and hybrid magmas; (4) deposition of mafic (basalts and andesitic basalts) and intermediate (andesites, dacites, and hybrid lavas) magmas occurred mainly in the form of lava flows, while sedimentation of felsic magma (rhyolites) was in the form of pyroclastic deposits (aerial fallout deposits, ignimbrites), domes, and rare lava flows of limited extension. Epiclastic deposits (conglomerates, sandstones, and siltstones) are mostly lenticular and limited in their extent. They indicate fluvial and/or lacustrine terrestrial sedimentary environments; (5) a very dispersed vent system was predominantly oriented parallel to the ESE–WNW fracture zone. Combined, these characteristics indicate a central volcano setting.

During the 2nd eruptive cycle, the Ediacaran volcanism in the TVF had the following volcanological characteristics: (1) eruptions also occurred in subaerial continental environments; (2) volcanism was characterized by the volumetric predominance of basaltic and andesitic magmas (basaltic andesites); andesites sensu stricto, dacites, and hybrid lavas were absent; (3) mafic eruptions occurred in the form of lava flows; (4) sedimentary deposits associated with this period are carbonates and siliciclastic deposits, indicating lacustrine and fluvial terrestrial environments. The fluvial sequences could have been very thick and of great lateral extent. These siliciclastic intervals thus reflect long periods of erosion between short-lived volcanic episodes; (5) contact of the basaltic succession with the underlying units is always marked by an angular unconformity; (6) volcanism occurred in an area located next to the margin of a continent, where a regional uplift was locally compensated by a subsidence, which occurred after volcanism cessation; (7) basaltic magmas have an anorogenic character and a tholeiitic affinity; (8) the closely spaced vent system was oriented parallel to the NE–SW structure, indicating a fissure-type volcanism.

During the late stage of the 2nd eruptive cycle, the Ediacaran volcanism of the TVF had the following volcanological characteristics: (1) eruptions also occurred in subaerial continental environments; (2) volcanism was characterized by the volumetric predominance of felsic magmas (rhyolites) expressed in the form of effusive rhyolitic bodies and a succession of deposits of pyroclastic flows (ignimbrites), which rest on various units of the underlying volcanic pile. The effusive rhyolitic bodies correspond to a short-distance lava flows (coulées) and domes associated with proximal deposits of pyroclastic flows and rhyolitic fall deposits.

The facies models that are the best match for the TVF are those associated with continental environments, namely: continental stratovolcanoes, continental basalt successions, and continental felsic volcanoes [111]. However, none of these models involves bimodal volcanism. Thus, the facies model for the TVF necessarily needs to combine these three facies models. The volcanological facies model of the TVF is that of a "continental stratovolcano" during the 1st volcanic cycle. The TVF then evolved to become compatible with the facies model of "continental basaltic successions" during the early stage of the 2nd eruptive cycle and finally with that of "continental felsic volcanoes" towards the end of the 2nd eruptive cycle.

5.3. Depositional Age of the TVF Volcanic Succession

The compilation of U-Pb zircon geochronological data for the igneous rocks of the Ouarzatate Group (i.e., CIMP) in the Central Anti-Atlas is summarized in Figure 12 and references to the publications where these ages were reported are compiled in Table S4.

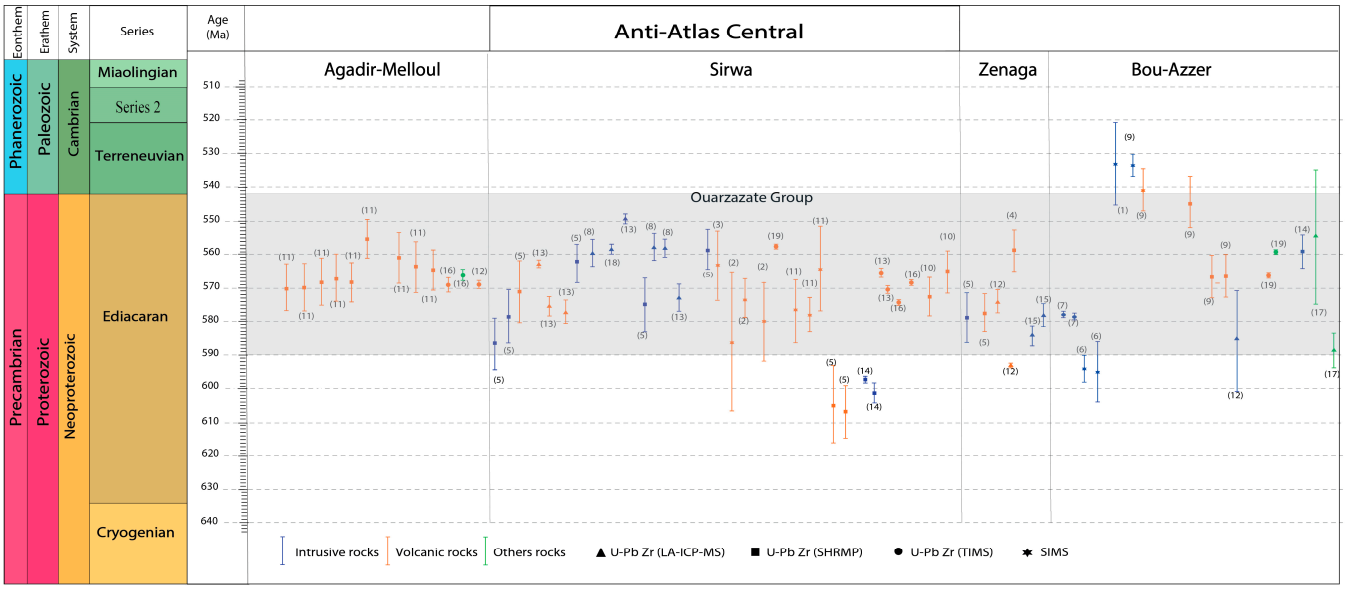

Figure 12. Compilation of available U–Pb geochronological ages for the Ediacaran volcanogenic units from the Central Anti-Atlas. The numbers refer to publications where these ages are reported (see Supplementary Materials Table S4).

The rhyolitic sample SI88 from the top of the 2nd eruptive cycle of the TVF (i.e., the top of the Ouazazate Group) yielded a weighted mean $^{206}Pb/^{238}U$ date of 557.613 ± 0.043 Ma (MSWD = 0.33, n = 5/6) on zircon analyzed by the CA-ID-TIMS method.

In the Siroua Window, on the northern margin of the Agadir Melloul Inlier, an ignimbrite sample yielded a weighted mean $^{206}Pb/^{238}U$ date of 575.0 ± 0.8 Ma (MSWD = 0.16, n = 3) on zircon analyzed by the CA-ID-TIMS method [33] and 572 ± 5 Ma on zircon analyzed by the SHRIMP method [24]: the sample OU72B of [33], described in [24] as a rhyolitic crystal tuff, TBOB647, from the base of the Adrar-n-Takoucht Formation (i.e., the basal part of the Ouazazate Group; Figure 13) that unconformably overlies the Wawkida Group (equivalent of the Tidilline Group of the Bou Azzer Inlier). Other samples from the same formation, OU71 and OU75 of [33], corresponding to well-stratified ash tuffs and massive ignimbrites, gave a weighted mean $^{206}Pb/^{238}U$ date 571.1 ± 1.1 Ma (MSWD = 1.4, n = 2) and 569.7 ± 0.7 Ma (MSWD = 0.82, n = 3; oldest dates) for zircons analyzed by the CA-ID-TIMS method, respectively.

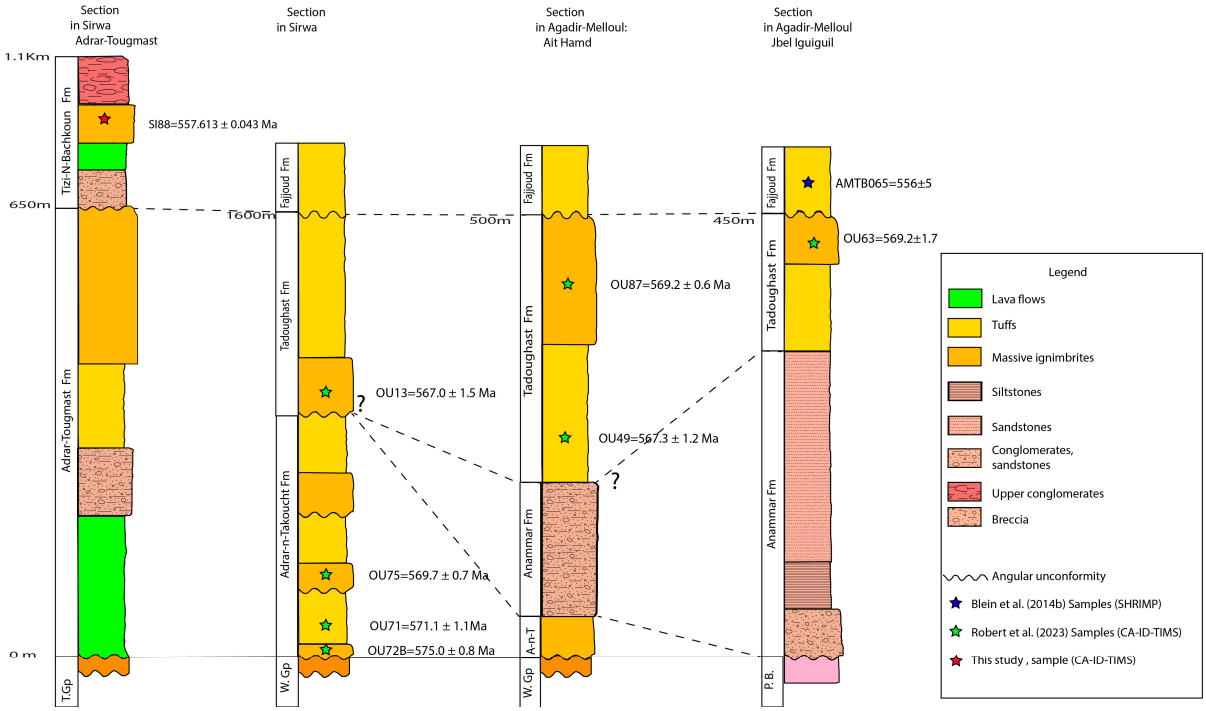

Figure 13. Stratigraphic columns for four sections of the TVF. The Adrar Tougmast section is from this study and the other three are from [33]. Sample dated by CA-ID-TIMS method in this study is shown with the red star; green stars [33] and blue stars [24] are for samples dated with the SHRIMP method. Abbreviations: P.B.: Paleoproterozoic bedrock; W.Gp: Wawkida Group; T.Gp: Tiddiline Group.

The sample OU13 [33], a crystal-rich pyroclastic tuff with a vitroclastic texture (TBTB329; [24]) from the Tadoughast Formation (Figure 13), yielded a weighted mean $^{206}Pb/^{238}U$ date of 567.0 ± 1.5 Ma (MSWD = 1.6, n = 4) on zircon analyzed by the CA-ID-TIMS method and 565 ± 6 Ma on zircon analyzed by the SHRIMP method [24].

In the Agadir Melloul Inlier, close to the Siroua Window, the sample OU49 (red hyaline tuff with a greater proportion of shards than crystal clasts) and sample OU87 (massive grey ignimbrite; [33]) from the same Tadoughast Formation (Ait Hamd Section) yielded a weighted mean $^{206}Pb/^{238}U$ date of 567.3 ± 1.2 Ma and a weighted mean 206Pb/238U age of 567.0 ± 1.5 Ma (MSWD = 0.64, n = 7) on zircon analyzed by the CA-ID-TIMS method, respectively. In the same section, an andesitic flow located below the massive ignimbrite of the Tadoughast Formation (Figure 13) yielded an age of 566 ± 6 Ma on zircon analyzed by the SHRIMP method (sample AMTB061) [24]. In the Jbel Iguiguil Section, the sample OU63 [33] from the same Tadoughast Formation yielded an age of 569.2 ± 1.7 Ma on zircon analyzed by the CA-ID-TIMS method.

A grey, welded massive lapilli tuff (sample AMTB065) gave a weighted mean age of 556 ± 5 Ma on zircon analyzed by the SHRIMP method [24]. This sample was collected in the Agadir Melloul Inlier near Jbel Iguiguil and belongs to the Fajjoud Formation. The lapilli tuff with a vitroclastic texture lacks lithic clasts and has only a few crystal clasts. The sample (located at the top of the unit) is stratigraphically equivalent to our rhyolitic sample SI88 at the top of the Ouarzazate Group and it yielded an age of 557.613 ± 0.043 Ma on zircon analyzed by the CA-ID-TIMS method.

Rhyolitic ignimbrites of High Irhiri (Siroua), corresponding to the base of the Ouarzazate Group, gave a Concordia zircon age of 580 ± 12 Ma by the ID-TIMS method [31]. This unit unconformably overlies the Amassine granite, which yielded a U-Pb age on zircon 661 ± 23 Ma by the SIMS method [31] and 601 ± 2 Ma and 599 ± 1 Ma by the SHRIMP method [112].

Rhyolites at the base of the Tikhfist Formation (Tiouin Subgroup) and the Aguins Member (Tawzzart Formation, Tafrant Subgroup), which are from the base and the top of the Ouarzazate Group volcanic succession, respectively, gave identical SHRIMP ages on zircon: 571 ± 8 Ma and 577 ± 6 Ma [19]. Both rhyolites belong to our 1st eruptive cycle of the TVF.

Zircon dates for the Zgounder rhyolitic domes, aligned E–W, cluster into four groups: (1) ca. 815 Ma date, corresponding to zircon's inherited cores reworked from the Neoproterozoic crust formed during the Pan-African, 885–555 Ma orogenic cycle [27]; (2) 610 ± 7 Ma; (3) 578 ± 4 Ma, corresponding to the emplacement of multiple rhyolitic intrusions and the large magma input to the upper crust of the Pan-African Orogen during the late Neoproterozoic; and (4) 564 ± 15 Ma, a less-precise date obtained on hydrothermally altered zircon domains in U-rich magmatic zircons. The latter date is the best estimate for the timing of hydrothermal albitization/mineralization in the Zgounder epithermal Ag–Hg deposit [32].

In the Tifnoute Valley, south of the Jbel Toubkal peak, rhyolite lava flows of the volcano-sedimentary succession of the Tachakoucht Formation, which corresponds to the base of the Ouarzazate Group according to [13], yielded a Concordia zircon age of 574 ± 2 Ma ([113]; LA-ICP-MS zircon method). A rhyodacitic ignimbrite and andesitic tuff of the andesitic volcanic succession of the Toubkal Massif, corresponding to the top of the volcanic pile of the Ouarzazate Group, have been dated by the LA-ICP-MS method on zircon at 577 ± 3 Ma and 562 ± 1 Ma, respectively [113].

The giant batholith of the Askaoun granodiorite has been dated at 575 ± 8 Ma by the SHRIMP method on zircon [19] and at 574 ± 3 Ma by the LA-ICP-MS method on zircon [113]. The Askaoun granodiorite also yielded a younger date on zircon at 558 ± 8 Ma ([114]; LA-ICP-MS method). The Imourkhssen granitic pluton, intruding the Askaoun granodiorite, has been dated at 562 ± 5 Ma ([19]; SHRIMP method on zircon), 561 ± 3 Ma ([114]; LA-ICP-MS method on zircon), and 558 ± 1 Ma ([16]; LA-ICP-MS method on zircon). The Ougougane granite, which corresponds to the felsic dyke of the Douar Eç-çour dyke swarm, yielded a date of 550 ± 1.5 Ma [16,113,115].

U-Pb zircon dates in Figure 12 and Table S4 were obtained by laser ablation–inductively coupled plasma–mass spectrometry (LA-ICP-MS), secondary ion mass spectrometry (SIMS)/sensitive high-resolution ion microprobe (SHRIMP), and chemical abrasion–isotope dilution–thermal ionization mass spectrometry (CA-ID-TIMS) techniques. The accuracy and precision of in situ U-Pb zircon dates obtained by the LA-ICP-MS, SIMS, and SHRIMP methods usually do not satisfy the requirements for high-resolution correlations among widely distributed rocks (e.g., [116]).

Based on the CA-ID-TIMS U-Pb zircon dates, the age of magmatism during deposition of the Ouarzazate Group in the Siroua Window can be bracketed between 575 ± 0.7 Ma, the age of the Adrar-n-Takoucht Formation [33], which could be the lateral equivalent of the Adrar Tougmast Formation of the TVF, and 557.613 ± 0.043 Ma, the age of the Tizi-n-Bachkoun Formation, obtained in this study, which could correspond to the Fajjoud Formation in the Agadir Melloul Inlier near Jbel Iguiguil ([24], Figure 13). The duration of the volcanic activity of the Ouarzazate Group could be estimated to be around 18 Myrs. The angular unconformity between the Adrar Tougmast and Tizi-n-Bachkoun formations of the TVF must be older than the 561 ± 6 Ma SHRIMP zircon U-Pb age for the Fajjoud Formation [24]. The age of the unconformity is thus estimated to be 560 Ma. This is the same as the age of the angular unconformity between the Lower and Upper Ouarzazate groups of Saghro [29]. It is uncertain how much time was taken by the hiatus along this unconformity, but it clearly has bearing on whether the two volcanic cycles of the TVF are genetically related.

5.4. Petrogenesis of the TVF

5.4.1. Fractional Crystallization vs. Crustal Contamination

The studied volcanics range in composition from ultramafic (2nd cycle) and mafic (1st cycle) to felsic, clearly indicating magma evolution through time.

Incompatible trace element ratios are largely unaffected by partial melting and fractional crystallization processes ([117] and references therein). The Zr vs. Nb diagram (Figure 14) shows that, except for rhyolites and ignimbrites of the 1st cycle, all the other lithologies of both cycles are characterized by Zr/Nb ratios of ≈20, suggesting that they are comagmatic, i.e., that they are derived from magmas generated from a common mantle source and later affected by closed-system magmatic evolution processes. The rhyolites and ignimbrites of the 1st cycle, having significantly lower Zr/Nb ratios (as low as 6.4), are clearly not comagmatic with other studied lithologies from the TVF in the Siroua Window.

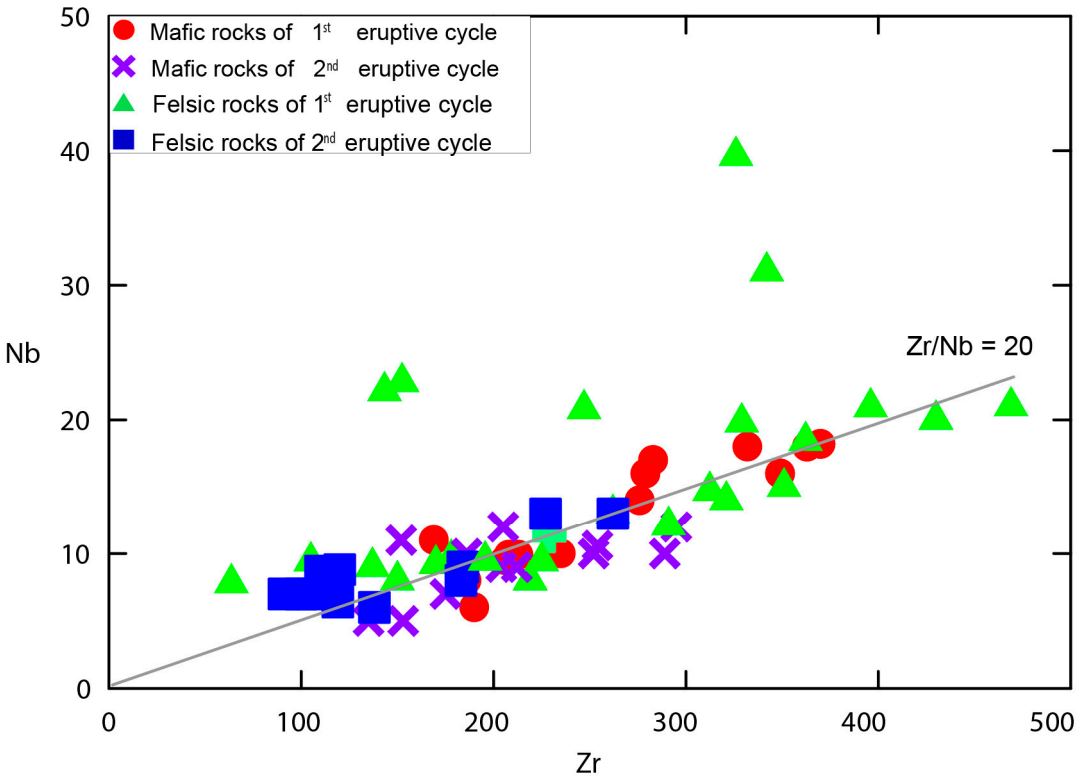

Figure 14. Zr vs. Nb diagram for the mafic and felsic rocks of TVF, showing the "Nb/Zr compatibility line" with Zr/Nb ≈20.

Even considering mafic rocks from both cycles (see Sections 4.3.2 and 4.3.3), the effects of magma evolution processes are evident. Indeed, taking into account Mg# up to 0.61 (1st cycle) and 0.50 (2nd cycle), even the most primitive rocks of the TVF are clearly not compatible with magmas generated in equilibrium with residual mantle mineralogy, i.e., primary magmas (Mg# = 0.68 to 0.75). This interpretation is also supported by low concentrations of transition trace elements (e.g., Ni ≤ 68 ppm; Cr ≤ 311 ppm) as compared with those typical for primary magmas (Cr ≥ 1000 ppm, Ni ≥ 400–500 ppm, Co ≥ 50–70 ppm; [118–120]; see Figure 15).

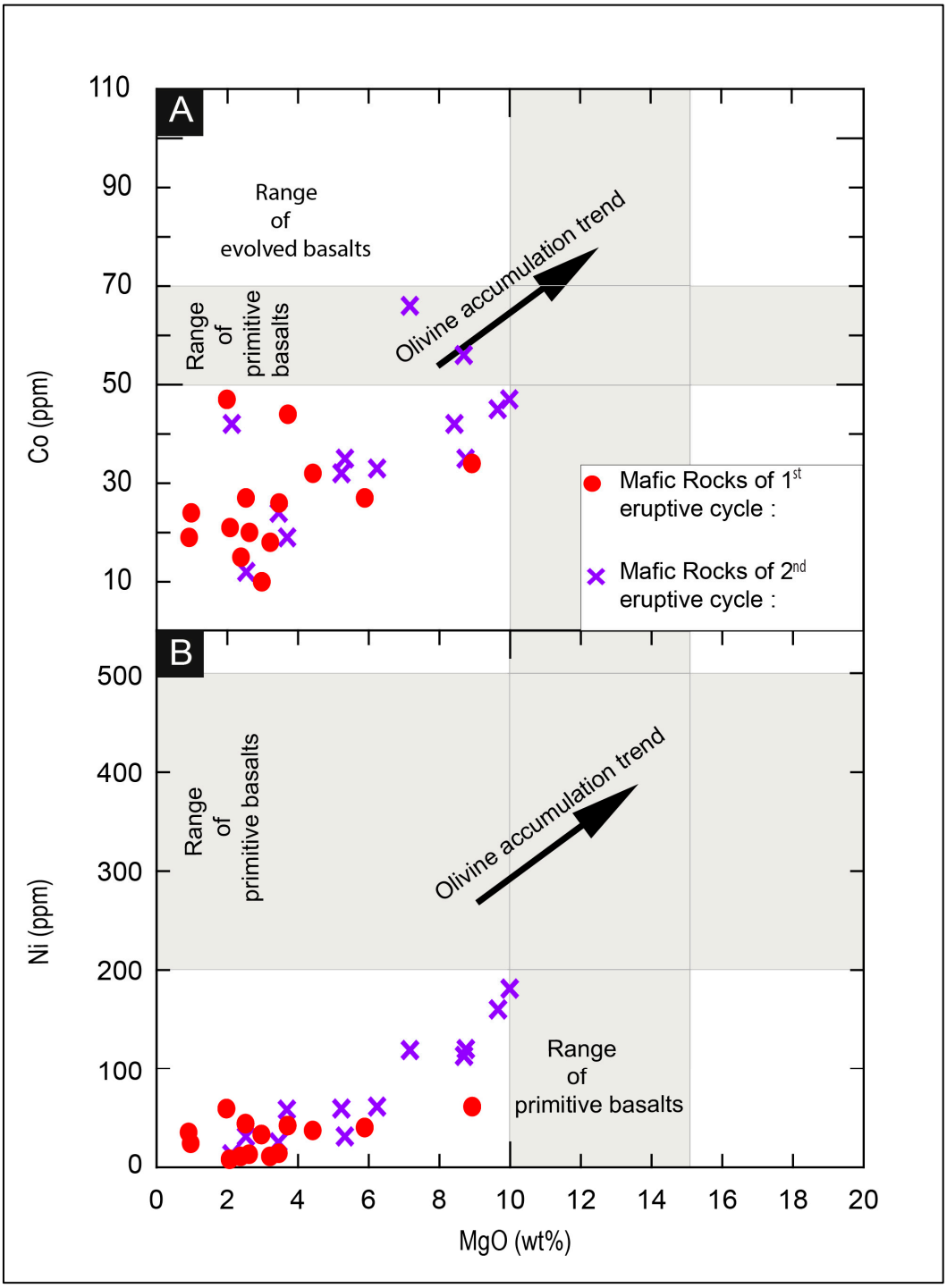

Figure 15. (**A**) MgO vs. Co; (**B**) MgO vs. Ni diagrams for the analyzed mafic rocks of the TVF of the Siroua Window. Ranges expected for magmas in equilibrium with their mantle sources: Ni = 200–500 ppm, Co = 50–70 ppm [121].

Thorium, as a highly incompatible element, can be used as an index for both partial melting and fractional crystallization processes [122–126]. Figure 16 shows inverse relation between Th and compatible elements, suggesting fractional crystallization rather than partial melting as the main cause of the chemical variability in the studied TVF volcanic rocks. Indeed, transition elements are known for their high compatibility with the ferromagnesian silicates (olivine and pyroxene) that first crystallize from mafic magmas [127], resulting in the lowering of their concentrations as fractional crystallization advances. For the chemical variation of mafic rocks, the role of plagioclase fractionation

was also important as evidenced by Sr and Eu negative anomalies (see Figure 8), which are accentuated in the felsic rocks (Figure 10). The felsic rocks are, in addition, characterized by significant Ti negative anomalies, whose meaning will be discussed later.

The diagrams of Figure 16 also show the role of partial melting in the generation of mafic magmas in the 2nd eruptive cycle.

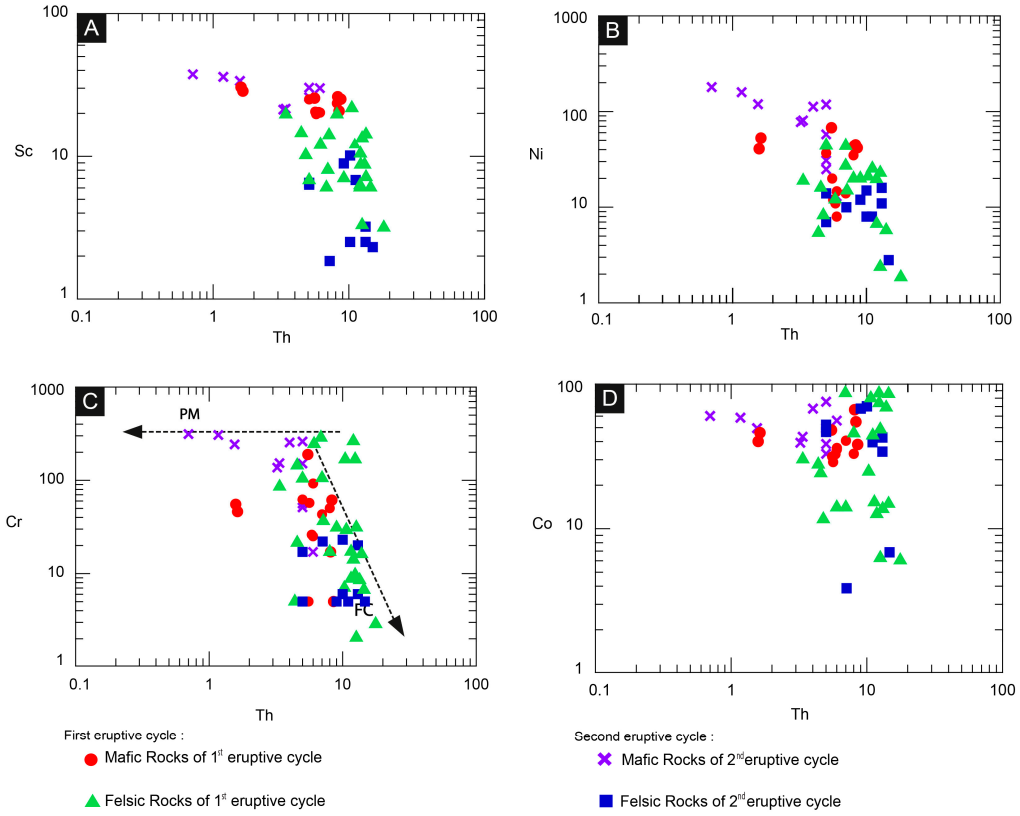

Figure 16. The Sc, Ni, Cr, and Co vs. Th diagrams (**A–D**; adapted from [125,127]), showing compositional variations in the volcanic and pyroclastic rocks from the TVF. PM—partial melting, FC—fractional crystallization.

One of the most striking characteristics of the mafic rocks of the TVF is the presence of pronounced Nb and Ta negative anomalies. The Nb depletion is also supported by the Nb/U ratios (Figure 17), which are clearly below the value of 47 ± 10 of MORB and OIB [128,129], i.e., of the oceanic basalts generated away from the influence of subduction processes.

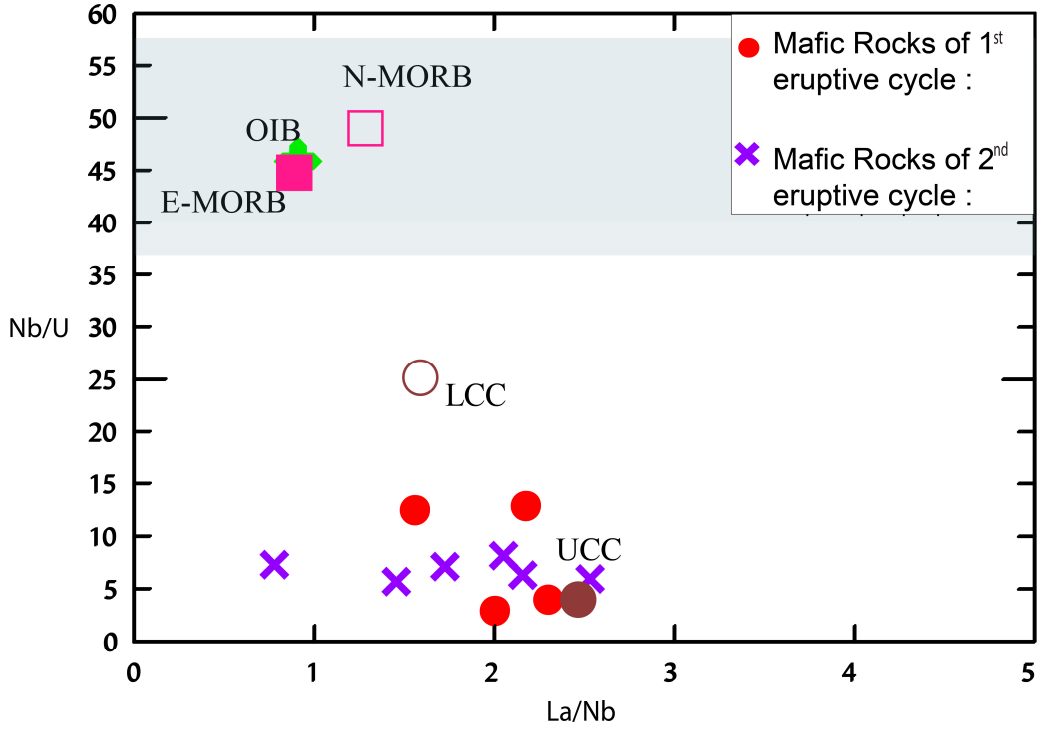

Figure 17. La/Nb vs. Nb/U for the analyzed mafic rocks with Mg# > 30 of the TVF of the Siroua Window. Data for the Upper Continental Crust (UCC) and Lower Continental Crust (LCC) are from [130]. Data for Oceanic Island Basalts (OIBs) and Mid-Ocean Ridge Basalts (MORBs) are from [105,128]. Shaded area corresponds to Nb/U = 47 ± 10 that characterizes oceanic magmas erupted away from the influence of subduction zones [128,129].

Since Nb and Ta are highly immobile in aqueous fluids generated by dehydration of subducting slabs [131,132], supra-subduction-related magmas are typically characterized by negative Nb and Ta anomalies [133], which translate, for example, to average Nb/U ratios of about 4.6 [134]. However, considering that the continental crust grows at the expense of arc magmas [135–137], an unavoidable consequence is that the Nb and Ta negative anomalies are also a characteristic of continental crust [138]. This makes it difficult to distinguish between the supra-subduction origin of the studied mafic rocks and the effects of basaltic magmas' contamination with crustal materials. However, at odds with arc magmas, continental crust is characterized by a P depletion, resulting in large negative anomalies (so called the "crust composition paradox" [139]). The lack of significant P negative anomalies, in association with strong negative Nb and Ta anomalies, is an indication of a metasomatized mantle enriched by subduction-related fluids rather than contamination by continental crust.

The fact that, except for the rhyolites and ignimbrites of the 1st cycle, all the other lithologies have similar Zr/Nb ratios (≈20) (Figure 14) suggests that even for the most evolved felsic rocks of the 2nd cycle the effects of crustal contamination were negligible. In this perspective, significant negative Ti anomalies shown by felsic rocks of the 2nd cycle are here linked to the crystallization of Ti-bearing oxides during magma evolution. The same conclusion can be extracted from the Zr/Hf ratios . Indeed, some of the felsic rocks of the 1st cycle are characterized by Zr/Hf values clearly lower than the chondritic value (≈38) presented by the 2nd cycle mafic to felsic rocks and by the mafic lithotypes of the 1st cycle.

5.4.2. Magma Source Composition and Magmatic Processes

From the above discussion, the source-inherited negative Nb and Ta anomalies must have been retained, which strongly points to a supra-subduction mantle source, metasomatized by aqueous fluids derived from a dehydrating subduction slab. This is further supported by the high normalized LILE/HFSE ratios for the mafic magmas (see Figure 8) and by the calc-alkaline characteristics of the mafic magmas inferred from clinopyroxene mineral chemistry (see Section 3.4; Figure 11).

As previously shown, even considering only the mafic rocks, the effects of fractional crystallization are evident. Olivine, clinopyroxene, and plagioclase were probably the dominant phases during the initial stages of crystallization. These phases do not significantly alter ratios involving elements incompatible with them, like Ce/Yb and La/Ta [105]. This allows the use of such ratios even for rocks with Mg# down to 30 to characterize signatures inherited from magma source processes. For values of Mg# inferior to 30, such ratios increase significantly as a result of magma evolution processes.

The Ce/Yb ratio of mantle magmas reflects melting pressure/depth, where high values indicate garnet involvement, owing to a significantly higher garnet distribution coefficient for Yb relative to Ce, at odds with that observed for the other common mantle residual phases, not capable of such significant Ce-Yb fractionation [140–142]. Consequently, partial melting of garnet peridotite yields Ce/Yb ratios exceeding 20 [143], while partial melting of spinel peridotite results in lower magma Ce/Yb ratios. Additionally, the distinction between asthenospheric and lithospheric magma sources can be informed by the La/Ta ratio [144–146]. Igneous rocks with La/Ta values < 22 are partial melts and inferred to be from asthenospheric sources with minimal or no lithospheric contamination, while [146] suggested that La/Ta ratios ranging from 22 to 30 might indicate lithospheric mantle contamination. The diagram Ce/Yb vs. La/Ta (Figure 18) suggests magma genesis close to the garnet–spinel peridotite zones mainly into the lithosphere.

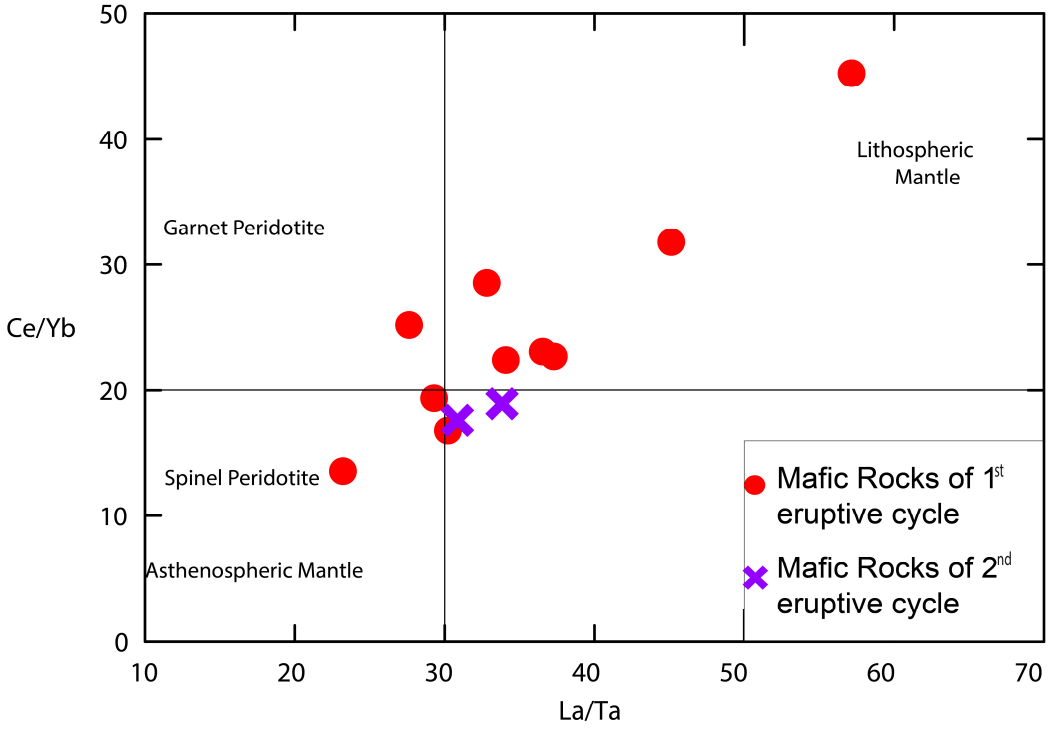

Figure 18. Ce/Yb vs. La/Ta diagram (based on values from [140–143] for the TVF mafic rocks with Mg# > 30).

The experimental work of [147,148] on the CMAS system indicates that the spinel–garnet transition occurs at ~2.4–2.5 GPa and 1440 °C, despite being dependent on peridotite fertility [149]. The positioning of TVF mafic rocks in Figure 18 suggests that primary magmas for most of the samples were generated at pressures around 2.5 GPa.

Since the two eruptive cycles are considered comagmatic here, as inferred from similar Zr/Nb ratios, the lower Th concentrations of the second eruptive cycle mafic rocks, compared to rocks with a similar degree of evolution of the first eruptive cycle (Figure 16), likely indicate a higher degree of partial melting.

This view is endorsed by the lower LREE concentrations of the 2nd cycle mafic rocks. Moreover, the variation in the extent of melting is also observed for a single cycle. Indeed, considering the mafic rocks of the 2nd cycle, a large range of Th contents, in association with high concentrations of compatible elements (Figure 16), suggests multiple and variable degrees of partial melting magmatic events. In summary, if most of the chemical variability in the studied rocks is due to fractional crystallization (see Section 5.4.1), a variable extent of partial melting events also contributed to the heterogeneity observed.

5.5. Tectonic Setting

The geochemistry of mafic rocks and of clinopyroxenes can be used, with caution, to constrain the tectonic setting that prevailed at the time of their emplacement (e.g., [134] and references therein). The TVF exposed in the Siroua Window of the Central Anti-Atlas belongs to the Ouarzazate Group ([11,19,24,31–33], this work). Two eruptive cycles are distinguished in the TVF, according to their volcanologic characteristics and geochemical signatures. The mafic rocks of both eruptive cycles carry pronounced Nb and Ta negative anomalies (see Section 5.4.1) and are characterized by high LILE/HFSE ratios (Figure 8), both interpreted as a signature of a magma source metasomatized by aqueous fluids associated with dehydration of a subduction plate. These characteristics correspond to the positioning of the studied mafic rocks in the tectonic setting discriminant plots of Figure 19 (see also Figure 11), where an orogenic (s.l.) setting is suggested. The tectonic setting of the TVF will be further refined taking into account their age and location of emplacement (see Section 5.6.2).

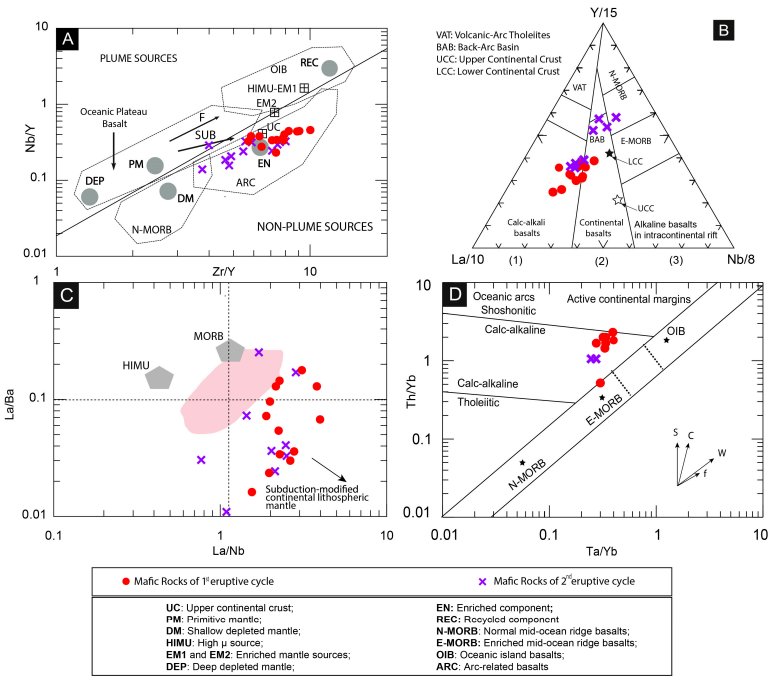

Figure 19. (**A**) Zr/Y vs. Nb/Y diagram [150], showing mantle compositional components and the mafic and intermediate rocks of the TVF. Arrows indicate effects of batch melting (F) and subduction (SUB). (**B**) Geochemical characterization of the TVF mafic and intermediate volcanic rocks in the La-Y-Nb diagram (after [151]). (**C**) La/Ba vs. La/Nb diagram (after [152]). The pink field represents subduction plate fluid-enriched arc basalts (after [153]). (**D**) Ta/Yb vs. Th/Yb diagram for the analyzed mafic rocks of the TVF of the Siroua Window (after [120]). Abbreviations: S: Contribution of subduction component; C: Crustal contamination; W: Within-plate component; f: Fractional crystallization. 1—orogenic domain; 2—intermediate domain (post-orogenic series with crustal contamination and "source effect"); 3—anorogenic domain.

5.6. Geodynamic Implications

The Pan-African Orogeny corresponds to a series of major Neoproterozoic mountain-building events that contributed to the formation of the Gondwana and Pannotia supercontinents about 600 million years ago (Figure 20).

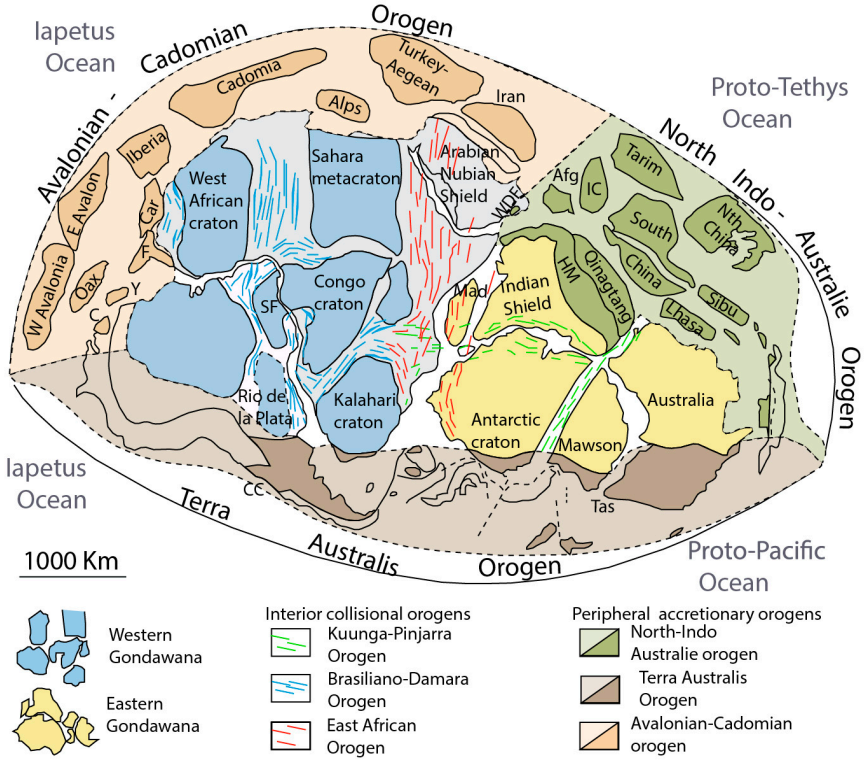

Figure 20. Map of Gondwana at ca. 500 Ma (after [154]), showing cratonic blocks and interior and peripheral orogens. The absolute and relative positions of most blocks within the peripheral orogens are poorly constrained and their positions depicted on this diagram are only indicative. Abbreviations: Afg—Afghanistan; C—Cortis; Car—Carolina; CC—Cuyania and Chilenia; Fl—Florida; IC—Indochina; HM—Himalayas; Mad—Madagascar; Oax—Oaxaquia; SF—San Francisco; TAS—Tasmania; WDF—Western Deformational Front; Y—Yucatan.

This orogenic cycle spans some 300 million years (most of the late Neoproterozoic), which is comparable to those during the assembly of the Columbia/Nuna and Rodinia (Grenville) supercontinents. This extended timeframe suggests that the Pan-African orogenic cycle consists of multiple orogenic episodes.

For comparison, the Cordilleran/Andean Orogeny, along the western margin of the Americas from Alaska to Chile, has developed over the past 380 million years, a duration comparable to that of the Pan-African orogenic cycle. However, the Cordilleran/Andean Orogeny includes six distinct episodes, each lasting between 30 and 90 million years, such

as the Antler (380–340 Ma), Sonoma (270–240 Ma), Nevada (180–140 Ma), Sevier (140–50 Ma), Laramide (70–35 Ma), and the ongoing Cascade and Andean orogenies. These episodes reflect different geodynamic settings, such as flat-slab subduction and collision with volcanic arcs and oceanic plateaus. The Cordilleran has been characterized as an accretionary orogeny [155], in contrast to the Pan-African Orogeny, which was primarily a collisional orogeny until the Ediacaran, when it was followed by the Cadomian accretionary orogenesis [156].

5.6.1. Previous Geodynamic Models

The Anti-Atlas Belt of Morocco is a key region for understanding Proterozoic accretion and break-up events along the margins of the West African Craton (WAC), given that a significant Pan-African Orogen segment is prominently exposed there. The Anti-Atlas Belt is considered to be a part of a 6000 km long Neoproterozoic "ring of fire" along the northern margin of the WAC [83]. This area contains extensive outcrops of the Neoproterozoic Pan-African Belt and the underlying Paleoproterozoic foreland, which have been intensely studied over many years (e.g., [13]). Traditionally, the Precambrian formations of the Anti-Atlas Belt have been divided into three major lithosomes (e.g., [13]): PI (Archean to Paleoproterozoic), PII (early and middle Neoproterozoic), and PIII (late Neoproterozoic) (Figure 1). However, this lithostratigraphic classification has recently been challenged [19,28,29,40,43–45,157].

In the new interpretation, the oldest Paleoproterozoic (PI) rocks in the Anti-Atlas Belt are divided into several complexes, such as the Zenaga and Kerdous (in the Siroua and Kerdous basement inliers). The overlying PII lithosome deposited on this basement is collectively referred to as the Anti-Atlas Supergroup, which consists of four volcano-sedimentary units (Lkest-Taghdout, Bou Azzer, Iriri, and Saghro), considered to be Neoproterozoic in age. Several intrusive suites (Ifzwane and Toudma) are also recognized, although they are still poorly dated. These volcano-sedimentary units have been associated with the early passive margin, oceanic, and island-arc environments, with ages ranging from 885 to 640 Ma. The earliest Pan-African deformation (660–640 Ma) is attributed to ocean basin closure, southwest-directed thrusting, and accretion of island-arc remnants [19,28,29,40].

Recent studies have provided new structural, geochronological, and geochemical data (e.g., [22,158]) and references therein). However, many critical questions about the accretionary history of the Anti-Atlas Belt are still debated (e.g., [158] and references therein). Such questions include the origin and tectonic framework of the Upper Ediacaran volcano-sedimentary cover series (i.e., the Ouarzazate Group), which unconformably overlies the deformed Pan-African units and immediately precedes the Ediacaran–Cambrian deposits that record the Basal Cambrian Carbon Isotope Excursion (BACE) [49].

Several models have been proposed for the origin and tectonomagmatic evolution of the Pan-African Anti-Atlas Belt (e.g., [12,19,29,30,83,159–170]). Previous models diverge on several aspects, particularly the early stages in the geodynamic evolution of the Pan-African Orogen. It is still unclear whether the subduction zone associated with accretion of an island arc dipped towards the north or towards the south. On the other hand, all these models (with the exception of the scheme of [161]) agree in that they consider the volcanism at the end of the Neoproterozoic as post-collisional (late-to-post-orogenic) and they link its origin to subduction of oceanic lithospheric plates; obducted ophiolites of Bou Azzer and Siroua are preserved remnants of these plates. The extensional stage (ca. 606–545 Ma) in the aftermath of the collision was marked by molasse deposition in a successor basin and igneous events (represented by the Ouarzazate Group), followed by the marine

transgression recorded by the Taroudant Group, which straddles the Ediacaran–Cambrian boundary.

5.6.2. Towards a New Geodynamic Model for the Ediacaran Magmatism in Morocco

The geological and geochronological data for the Ediacaran volcanic rocks from the TVF of the Siroua Window in the Anti-Atlas Belt indicate that the volcanism occurred at ca. 575–557 Ma (based on TIMS zircon U-Pb data; [33] and this study). Considering that the collisional processes in the Pan-African Orogen may have occurred at approximately 647 Ma [34], such ages confer a post-collisional setting to the studied TVF. Volcanic eruptions occurred in a continental setting [16,24,32,33,113] in two successive, eruptive cycles distinguished according to their volcanological characteristics and geochemical signatures (see above).

The post-collisional timing of the TVF volcanism impedes its genetic relation with coeval active subduction event(s). This post-collisional magmatism suggests that an orogenic collapse following collision led to gravitational and thermal instability of the lithosphere, inducing magmatism [3]. Such melting events would be facilitated by the existence of low-solidus metasomatized lithospheric domains imprinted by fluids generated during previous subduction processes (e.g., [171]). This scenario explains the geochemical characteristics of the TVF, namely the Nb-Ta negative anomalies and the high LILE/HFSE ratios (Figure 8).

In general, two models have been proposed to explain post-collisional magmatism associated with an orogen collapse: lithospheric delamination and convective erosion [3,4,172–178], both leading to a reduction in lithosphere thickness. This lithospheric thickness reduction/thinning is also imperative in the present case. Indeed, some melts were generated at the spinel–garnet transition, at pressure close to 2.5 GPa (see Section 5.4.2). Considering a crustal thickness of about 40 km and mean density of the crust and lithospheric mantle of 2700 kg/m^3 and 3200 kg/m^3, respectively, such pressure would correspond to ~84 km in depth. This depth is likely significantly shorter than the thickness of the lithosphere in the aftermath of collision, thus requiring significant thickness reduction in order to make it feasible for lithospheric melting at ~84 km in depth by interaction with the hotter asthenosphere. The oldest mafic TVF magmatism is dated at 575 Ma, i.e., some 72 Ma after the end of collision [59]. This suggests a long-lasting process of lithospheric thinning (s.l.) before melting started.

No single model can explain all the events in the Anti-Atlas collisional belt. Figure 21 illustrates our proposed model for the unroofing and collapse in the collisional orogen of the Pan-African Anti-Atlas Belt: (1) oceanic crust subduction between ca. 777 and 760 Ma ago released fluids from a dehydrating subduction plate [59] that metasomatized the overlying asthenosphere and lithosphere mantle. (2) Continental collision between the West African Craton and the northern block led to continental subduction and subsequent exhumation with syn-collisional magmatism at ca. 650–640 Ma (; e.g., [179]). (3) As a consequence of orogenic collapse, the lithospheric mantle has been thinned. (4) A reduction in the lithospheric thickness and increase in heat transfer from the asthenosphere with magmatism started at ca. 575 Ma and continued for ca. 15 million years (until ca. 560 Ma). (5) Associated delamination of the lithospheric mantle and consequent isostatic adjustment ended with complete leveling of the orogen and deposition of the shallow-marine, mixed siliciclastic–carbonate sequence of the late Ediacaran–early Cambrian Taroudant Group, which marks the end of the Pan-African orogenic cycle.

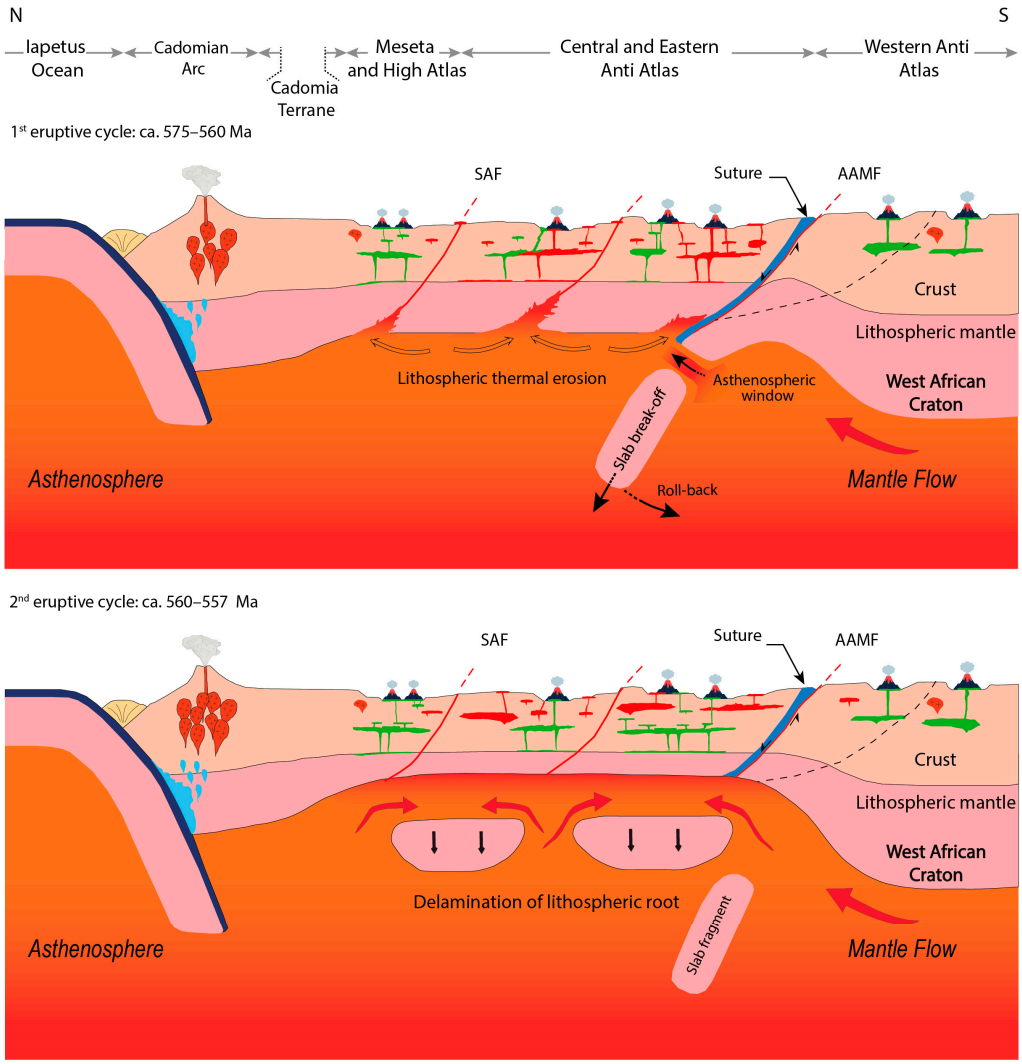

Figure 21. Tectonomagmatic model for the Moroccan Ediacaran illustrating the setting of two eruptive cycles in the late Neoproterozoic in the Anti-Atlas and High-Atlas–Meseta–Cadomian Arc that shows the process of lithospheric mantle delamination, which led to the post-collisional magmatism of the second eruptive cycle. Inspired by the general model of [12,172,175]. SAF—South Atlas Fault. AAMF—Anti-Atlas Major Fault.

The delamination model suggests that the dense base of an orogenically thickened continental lithosphere detached and sank into the asthenosphere. Numerical modeling [172] suggests that a tectonic event could have initiated an elongated conduit connecting the hot asthenosphere to the crustal base, creating a localized thermal anomaly that facilitates voluminous crustal melting. This process may explain formation of the felsic rocks from the first eruptive cycle. However, felsic rocks of the second cycle, with Zr/Nb ratios similar to the associated mafic rocks, are more likely to result from fractional crystallization rather than crustal melting.

In the Siroua Window (Central Anti-Atlas), lithospheric instabilities could have occurred near the end of early Pan-African subduction (ca. 762 Ma ago) due to slab break-off or rollback, potentially coupled with the gravitational collapse of the Central Anti-Atlas block. While delamination is a widely discussed mechanism for forming large igneous provinces [180], applying this model to the Pan-African Belt requires further careful consideration of its temporal and geochemical complexities [178].

6. Concluding Remarks

1. According to their volcanological, stratigraphical, and geochemical characteristics, two consecutive eruptive cycles can be distinguished in the Taghdout Volcanic Field (TVF) of the Ouarzazate Group exposed in the Siroua Window (Anti-Atlas Belt).

2. The precise geochronological dating of the FVF rocks (575 Ma to 557 Ma) allows for assigning them to a post-collisional stage in the Pan-African Orogen evolution.

3. Mafic subalkaline (calc-alkaline) magmas clearly show chemical characteristics indicative of sources metasomatized by fluids derived from dehydrating subduction slab(s), likely in the aftermath of the Pan-African Orogeny.

4. Mafic rocks that erupted over a period of ca. 18 Ma evolved from primary magmas originated by melting of a peridotitic lithospheric mantle during collapse of the Pan-African Orogen. Chemical composition of post-collisional mafic magmatism evolved systematically over time with the mafic rocks of the first eruptive cycle (ca. 575 to 560 Ma) being derived from magmas with a lower degree of partial melting than those of the second cycle (ca. 557 Ma), suggesting an increased heat transfer from asthenosphere associated with its upwelling.

5. Our model implies a significant reduction in the lithospheric thickness during the orogenic collapse, probably involving a long-lived, sublithospheric thermal erosion, followed by a rapid delamination causing a large-scale, isostatic adjustment. Afterwards, surface relief diminished and Ediacaran–Cambrian, mixed siliciclastic–carbonate sediments covered the craton, recording the end of the Pan-African orogenic cycle, the Ediacaran–Cambrian transition, and the Basal Cambrian Carbon Isotope Excursion (BACE).

Supplementary Materials: The following supporting information can be downloaded at: https://www.mdpi.com/article/10.3390/min15020142/s1, Table S1 CA-ID-TIMS zircon U-Th-Pb data for SI88 samples collected from the upper part of the Taghdout Volcanic Field (TVF) volcanic pile in the Siroua Window, Anti-Atlas. (GPS WGS84: latitude: N 30.7243025; longitude: W-7.3625674). Table S2. Database of whole-rock major and trace element geochemical data for the Ediacaran effusive and pyroclastic units of the Taghdout Volcanic Field (TVF) in the Siroua Window, Anti-Atlas. The geochemical database is from this work (samples with asterisk), unpublished theses of two co-authors [14,97] and literature data are from two unpublished theses of [98,99]. Loss-on-ignition (L.O.I.) determined by weight loss after ignition of the sample at 1000 °C. Table S3. Selected representative electron microprobe analyses of clinopyroxene from basaltic andesite of the Adrar Tougmast Formation (sample YS 60) and basalt of the Tizi-n-Bachkoun Formation (sample YS 22). Table S4. Database of U-Pb geochronological data from the Ouarzazate Group in the Central Anti-Atlas, Morocco. Radiometric dates are tabulated as reported in the original literature. No corrections have been made with regard to decay constant, standard calibration, and trace calibration. After the compilation of [11] completed by this work.

Author Contributions: Conceptualization, M.A.M., N.Y. and I.H.; methodology, M.A.M., N.Y. and J.-F.W.; software, M.A.M., O.M. and I.H.; validation, N.Y., J.M. (João Mata), J.M. (José Madeira), M.D., E.E.D.A.H.K., W.E.M., A.A.L., M.A.B. and A.B.; formal analysis, M.A.M., N.Y., O.M. and I.H.; investigation, M.A.M., N.Y. and M.B.C.; resources, N.Y.; data curation, M.A.M., N.Y. and M.B.C.; writing—original draft preparation, M.A.M., N.Y. and I.H.; writing—review and editing, J.M. (João Mata), J.M. (José Madeira), M.D., E.E.D.A.H.K., J.-F.W. and A.B.; visualization, R.O. and J.O.; supervision, N.Y. and M.A.B.; project administration, M.A.B.; funding acquisition, N.Y. and A.B. All authors have read and agreed to the published version of the manuscript.

Funding: This research was funded by the Petroleum Foundation of the American Chemical Society, grant number "624840ND2" and the Portuguese Fundação para a Ciência e a Tecnologia (FCT) I.P./MCTES through national funds (PIDDAC)—UIDB/50019/2020-IDL.

Data Availability Statement: Data are contained within the article and supplementary materials.

Acknowledgments: Most of this work was carried out at the Department of Geology of the Faculty of Sciences-Semlalia, Cadi Ayyad University of Marrakech, "Laboratoire de Géochimie Comparée et Systématique of Université Pierre et Marie Curie—Paris 6 (UPMC)", and Centre de Recherches Pétrographiques et Géochimiques (CRPG) de Nancy. João Mata and José Madeira were funded by the Portuguese Fundação para a Ciência e a Tecnologia (FCT) I.P./MCTES through national funds (PIDDAC)—UIDB/50019/2020-IDL. Andrey Bekker was supported by the Petroleum Foundation of the American Chemical Society, grant 624840ND2. Warda El Moume, Abdelhak Ait Lahna, Moulay Ahmed Boumehdi, and Nasrrddine Youbi were supported by the APRD project "AlkaCarboLipsWac" "Proterozoic and Phanerozoic Alkaline Igneous Rocks and Carbonatites and associated LIPs of the West African Craton (Morocco, Mauritania, and Mali) and their potential for Nb, Ta, U, REE, Fe, Phosphates, and other Ore Deposits", (Leader Prof. Nasrrddine Youbi) and funded by the OCP Fondation (Office Chérifien des Phosphates), UM6P (Mohamed VI Polytechnic University of Benguerir), CNRST (National Center for Scientific and Technical Research, Rabat), and MESRSI (Ministry of Higher Education, Research and Innovation, Rabat).

Conflicts of Interest: The authors declare no conflicts of interest.

References

1. Liegeois, J.-P.; Navez, J.; Hertogen, J.; Black, R. Contrasting Origin of Post-Collisional High-K Calc-Alkaline and Shoshonitic versus Alkaline and Peralkaline Granitoids. The Use of Sliding Normalization. *Lithos* **1998**, *45*, 1–28. https://doi.org/10.1016/S0024-4937(98)00023-1
2. Song, S.G.; Wang, M.J.; Wang, C.; Niu, Y.L. Magmatism during Continental Collision, Subduction, Exhumation and Mountain Collapse in Collisional Orogenic Belts and Continental Net Growth: A Perspective. *Sci. China Earth Sci.* **2015**, *58*, 1284–1304. https://doi.org/10.1007/s11430-015-5102-x.
3. Zhou, C.A.; Song, S.; Allen, M.B.; Wang, C.; Su, L.; Wang, M. Post-Collisional Mafic Magmatism: Insights into Orogenic Collapse and Mantle Modification from North Qaidam Collisional Belt, NW China. *Lithos* **2021**, *398–399*, 106311. https://doi.org/10.1016/j.lithos.2021.106311.
4. Wang, Q.; Zhao, J.; Zhang, C.; Yu, S.; Ye, X.; Liu, X. Paleozoic Post-Collisional Magmatism and High-Temperature Granulite-Facies Metamorphism Coupling with Lithospheric Delamination of the East Kunlun Orogenic Belt, NW China. *Geosci. Front.* **2022**, *13*, 101271. https://doi.org/10.1016/j.gsf.2021.101271.
5. Macdonald, F.A.; Yonkee, W.A.; Flowers, R.M.; Swanson-Hysell, N.L. Neoproterozoic of Laurentia. *Mem. Geol. Soc. Am.* **2023**, *220*, 331–380. https://doi.org/10.1130/2022.1220(19).
6. Puffer, J.H. A Late Neoproterozoic Eastern Laurentian Superplume: Location, Size, Chemical Composition, and Environmental Impact. *Am. J. Sci.* **2002**, *302*, 1–27. https://doi.org/10.2475/ajs.302.1.1.
7. Mitchell, R.N.; Kilian, T.M.; Raub, T.D.; Evans, D.A.D.; Bleeker, W.; Maloof, A.C. Sutton Hotspot: Resolving Ediacaran-Cambrian Tectonics and True Polar Wander for Laurentia. *Am. J. Sci.* **2011**, *311*, 651–663. https://doi.org/10.2475/08.2011.01.
8. Shumlyanskyy, L.; Nosova, A.; Billström, K.; Söderlund, U.; Andréasson, P.G.; Kuzmenkova, O. The U–Pb Zircon and Baddeleyite Ages of the Neoproterozoic Volyn Large Igneous Province: Implication for the Age of the Magmatism and the Nature of a Crustal Contaminant. *GFF* **2016**, *138*, 17–30. https://doi.org/10.1080/11035897.2015.1123289.
9. Tegner, C.; Andersen, T.B.; Kjøll, H.J.; Brown, E.L.; Hagen-Peter, G.; Corfu, F.; Planke, S.; Torsvik, T.H. A Mantle Plume Origin for the Scandinavian Dyke Complex: A "Piercing Point" for 615 Ma Plate Reconstruction of Baltica? *Geochem. Geophys. Geosystems* **2019**, *20*, 1075–1094. https://doi.org/10.1029/2018GC007941.
10. Poprawa, P.; Krzemińska, E.; Pacześna, J.; Amstrong, R. Geochronology of the Volyn Volcanic Complex at the Western Slope of the East European Craton—Relevance to the Neoproterozoic Rifting and the Break-up of Rodinia/Pannotia. *Precambrian Res.* **2020**, *346*, 105817. https://doi.org/10.1016/j.precamres.2020.105817.
11. Youbi, N.; Ernst, R.E.; Söderlund, U.; Boumehdi, M.A.; Lahna, A.A.; Tassinari, C.C.G.; El Moume, W.; Bensalah, M.K. The Central Iapetus Magmatic Province: An Updated Review and Link with the ca. 580 Ma Gaskiers Glaciation. *Spec. Pap. Geol. Soc. Am.* **2020**, *544*, 35–66. https://doi.org/10.1130/2020.2544(02).
12. Ousbih, M.; Ikenne, M.; Cousens, B.; Chelle-Michou, C.; El Bilali, H.; Gaouzi, A.; Markovic, S.; Askkour, F.; Mouhajir, M.; El Mouden, S.; et al. Stratigraphy, Geochronology, Geochemistry and Nd Isotopes of the Ouarzazate Group, Anti-Atlas, Morocco:

Evidence of a Late Neoproterozoic LIP in the Northwestern Part of the West African Craton. *Lithos* **2024**, *474–475*, 107593. https://doi.org/10.1016/j.lithos.2024.107593.

13. Choubert, G. Histoire Géologique Du Précambrien de l'Anti-Atlas. *Notes Et Mém. Serv. Géol. Maroc* **1963**, *1*, 352.
14. Youbi, N. Le Volcanisme «Post-Collisionnel»: Un Magmatisme Intraplaque Relié à Des Panaches Mantelliques. Etude Volcanologique et Géochimique. Exemples d'Application Dans Le Néoprotérozoïque Terminal (PIII) de L'Anti-Atlas et Le Permien du Maroc. Ph.D. thesis, Faculty of Sceinces Semlalia, University Cadi Ayyad, Marrakesh, Morocco, 1998
15. Belkacim, S.; Gasquet, D.; Liégeois, J.P.; Arai, S.; Gahlan, H.A.; Ahmed, H.; Ishida, Y.; Ikenne, M. The Ediacaran Volcanic Rocks and Associated Mafic Dykes of the Ouarzazate Group (Anti-Atlas, Morocco): Clinopyroxene Composition, Whole-Rock Geochemistry and Sr-Nd Isotopes Constraints from the Ouzellarh-Siroua Salient (Tifnoute Valley). *J. Afr. Earth Sci.* **2017**, *127*, 113–135. https://doi.org/10.1016/j.jafrearsci.2016.08.002.
16. Ferraq, M.; Belkacim, S.; Cheng, L.-Z.; Davies, J.H.F.L.; Perrot, M.G.; Ben-Tami, A.; Bouabdellah, M. New Geochemical and Geochronological Constraints on the Genesis of the Imourkhssen Cu ± Mo ± Au ± Ag Porphyry Deposit (Ouzellagh-Siroua Salient, Anti-Atlas, Morocco): Geodynamic and Metallogenic Implications. *Minerals* **2024**, *14*, 832. https://doi.org/10.3390/min14080832.
17. Piqué, A.; Bouabdelli, M.; Soulaïmani, A.; Youbi, N.; Iliani, M. Les Conglomerats Du P III (Neoproterozoique Superieur) de l'Anti Atlas (Sud Du Maroc): Molasses Panafricaines, Ou Marqueurs d'un Rifting Fini-Proterozoique? *Comptes Rendus L'academie Sci.—Ser. IIa Sci. La Terre Des Planetes* **1999**, *328*, 409–414. https://doi.org/10.1016/S1251-8050(99)80107-4.
18. Doblas, M.; López-Ruiz, J.; Cebriá, J.M.; Youbi, N.; Degroote, E. Mantle Insulation beneath the West African Craton during the Precambrian-Cambrian Transition. *Geology* **2002**, *30*, 839–842. https://doi.org/10.1130/0091-7613(2002)030<0839:MIBTWA>2.0.CO;2.
19. Thomas, R.J.; Chevallier, L.P.; Gresse, P.G.; Harmer, R.E.; Eglington, B.M.; Armstrong, R.A.; De Beer, C.H.; Martini, J.E.J.; De Kock, G.S.; Macey, P.H.; et al. Precambrian Evolution of the Sirwa Window, Anti-Atlas Orogen, Morocco. *Precambrian Res.* **2002**, *118*, 1–57. https://doi.org/10.1016/S0301-9268(02)00075-X.
20. Pouclet, A.; Tchameni, R.; Mezger, K.; Vidal, M.; Nsifa, E.; Shang, C.; Penaye, J. Archaean Crustal Accretion at the Northern Border of the Congo Craton (South Cameroon). *The Charnockite-TTG Link. Bull. La Soc. Geol. Fr.* **2007**, *178*, 331–342. https://doi.org/10.2113/gssgfbull.178.5.331.
21. Gasquet, D.; Levresse, G.; Cheilletz, A.; Azizi-Samir, M.R.; Mouttaqi, A. Contribution to a Geodynamic Reconstruction of the Anti-Atlas (Morocco) During Pan-African Times with the Emphasis on Inversion Tectonics and Metallogenic Activity at the Precambrian-Cambrian Transition. *Precambrian Res.* **2005**, *140*, 157–182. https://doi.org/10.1016/j.precamres.2005.06.009.
22. Gasquet, D.; Ennih, N.; Liégeois, J.-P.; Soulaimani, A.; Michard, A. The Pan-African belt. In Continental Evolution: The Geology of Morocco; Michard, A., Saddiqi, O., Chalouan, A., de Lamotte, D.F., Eds.; Lecture Notes in Earth Sciences; Springer: Berlin/Heidelberg, Germany, 2008; Volume 116, pp. 33–64. doi.org/10.1007/978-3-540-77076-3_2.
23. Blein, O.; Baudin, T.; Chèvremont, P.; Soulaimani, A.; Admou, H.; Gasquet, P.; Cocherie, A.; Egal, E.; Youbi, N.; Razin, P.; et al. Geochronological Constraints on the Polycyclic Magmatism in the Bou Azzer-El Graara Inlier (Central Anti-Atlas Morocco). *J. Afr. Earth Sci.* **2014**, *99*, 287–306. https://doi.org/10.1016/j.jafrearsci.2014.04.021.
24. Blein, O.; Baudin, T.; Soulaimani, A.; Cocherie, A.; Chèvremont, P.; Admou, H.; Ouanaimi, H.; Hafid, A.; Razin, P.; Bouabdelli, M.; et al. New Geochemical, Geochronological and Structural Constraints on the Ediacaran Evolution of the South Sirwa, Agadir-Melloul and Iguerda Inliers, Anti-Atlas, Morocco. *J. Afr. Earth Sci.* **2014**, *98*, 47–71. https://doi.org/10.1016/j.jafrearsci.2014.06.019.
25. Cheilletz, A.; Levresse, G.; Gasquet, D.; Azizi-Samir, M.; Zyadi, R.; Archibald, D.A.; Farrar, E. The Giant Imiter Silver Deposit: Neoproterozoic Epithermal Mineralization in the Anti-Atlas, Morocco. *Miner. Depos.* **2002**, *37*, 772–781. https://doi.org/10.1007/s00126-002-0317-0.
26. Tuduri, J.; Chauvet, A.; Barbanson, L.; Labriki, M.; Dubois, M.; Trapy, P.H.; Lahfid, A.; Poujol, M.; Melleton, J.; Badra, L.; et al. Structural Control, Magmatic-Hydrothermal Evolution and Formation of Hornfels-Hosted, Intrusion-Related Gold Deposits: Insight from the Thaghassa Deposit in Eastern Anti-Atlas, Morocco. *Ore Geol. Rev.* **2018**, *97*, 171–198. https://doi.org/10.1016/j.oregeorev.2018.04.023.
27. Ait Lahna, A.; Youbi, N.; Tassinari, C.C.G.; Basei, M.A.S.; Ernst, R.E.; Chaib, L.; Barzouk, A.; Mata, J.; Gärtner, A.; Admou, H.; et al. Revised stratigraphic framework for the lower Anti-Atlas supergroup based on U–Pb geochronology of magmatic and detrital zircons (Zenaga and Bou Azzer-El Graara inliers, Anti-Atlas belt, Morocco). *J. Afr. Earth Sci.* **2020**, *171*, 103946. https://doi.org/10.1016/j.jafrearsci.2020.103946.

28. Thomas, R.J.; Fekkak, A.; Ennih, N.; Errami, E.; Loughlin, S.C.; Gresse, P.G.; Chevallier, L.P.; Liégeois, J.P. A New Lithostratigraphic Framework for the Anti-Atlas Orogen, Morocco. *J. Afr. Earth Sci.* **2004**, *39*, 217–226. https://doi.org/10.1016/j.jafrearsci.2004.07.046.
29. Walsh, G.J.; Benziane, F.; Aleinikoff, J.N.; Harrison, R.W.; Yazidi, A.; Burton, W.C.; Quick, J.E.; Saadane, A. Neoproterozoic Tectonic Evolution of the Jebel Saghro and Bou Azzer-El Graara Inliers, Eastern and Central Anti-Atlas, Morocco. *Precambrian Res.* **2012**, *216–219*, 23–62. https://doi.org/10.1016/j.precamres.2012.06.010.
30. Blein, O.; Baudin, T.; Chevremont, P.; Gasquet, D. Petrogenesis of Late Ediacaran Volcanic Rocks of the Kerdous and Tagragra d'Akka Inliers (Anti-Atlas Morocco): Involvement of Slab-Failure. *J. Afr. Earth Sci.* **2023**, *199*, 104831. https://doi.org/10.1016/j.jafrearsci.2023.104831.
31. Mifdal, A.; Peucat, J.-J. Datations U-Pb et Rb-Sr Du Volcanisme Acide de l'Anti-Atlas Marocain et Du Socle Sous-Jacent Dans La Région de Ouarzazate. Apport Au Problème de La Limite Précambrien-Cambrien. U-Pb and Rb-Sr Dating of Acidic Volcanic Rocks and Precambrian Basement in Ant. *Sci. Géologiques. Bull.* **1985**, *38*, 185–200. https://doi.org/10.3406/sgeol.1985.1706.
32. Pelleter, E.; Cheilletz, A.; Gasquet, D.; Mouttaqi, A.; Annich, M.; Camus, Q.; Deloule, E.; Ouazzani, L.; Bounajma, H.; Ouchtouban, L. U/Pb Ages of Magmatism in the Zgounder Epithermal Ag–Hg Deposit, Sirwa Window anti-atlas, Morocco mineral deposits of north Africa. Miner. Res. Rev, 2016; pp. 143–165. https://doi.org/10.1007/978-3-319-31733-5_5.
33. Robert, B.; Corfu, F.; Domeier, M.; Blein, O. Evidence for Large Disturbances of the Ediacaran Geomagnetic Field from West Africa. *Precambrian Res.* **2023**, *394*, 107095. https://doi.org/10.1016/j.precamres.2023.107095.
34. Inglis, J.; Hefferan, K.; Samson, S.; Admou, H.; Saquaque, A. Determining age of Pan African metamorphism using Sm-Ndgarnet-whole rock geochronology and phase equilibria modeling in the Tasriwine ophiolite, Sirwa, Anti-Atlas, Morocco. *J. Afr.Earth Sci.* **2016**, *127*, 88–98. https://doi.org/10.1016/j.jafrearsci.2016.06.021.
35. Thieblemont, D. An updated geological map of Africa at 1:10,000,000 scale. In Proceedings of the 35th International Geological Congress (IGC 2016), Cape Town, South Africa, 27 August–4 September 2016.
36. Brahimi, S.; Liégeois, J.P.; Ghienne, J.F.; Munschy, M.; Bourmatte, A. The Tuareg Shield Terranes Revisited and Extended towards the Northern Gondwana Margin: Magnetic and Gravimetric Constraints. *Earth-Sci. Rev.* **2018**, *185*, 572–599. https://doi.org/10.1016/j.earscirev.2018.07.002.
37. Ennih, N.; Liégeois, J.-P. The Moroccan Anti-Atlas: The West African Craton Passive Margin with Limited Pan-African Activity. Implications for the Northern Limit of the Craton. *Precambrian Res.* **2001**, *112*, 289–302. https://doi.org/10.1016/S0301-9268(01)00195-4.
38. Liégeois, J.P.; Fekkak, A.; Bruguier, O.; Errami, E.; Ennih, N.; J.P.; Liégeois, A.; Fekkak, O.; Bruguier, E.; Errami, N.E. The Lower Ediacaran (630–610 Ma) Saghro Group: An Orogenic Transpressive Basin Development During the Early Metacratonic Evolution of the Anti-Atlas (Morocco). In Proceedings of the IGCP485 4th Meeting, Algiers, Algeria, 2 September 2006; p.57.
39. Malek, H.A.; Gasquet, D.; Bertrand, J.M.; Leterrier, J. Geochronologie U-Pb Sur Zircon de Granitoides Eburneens et Panafricains Dans Les Boutonnieres Proterozoiques d'Igherm, Du Kerdous et Du Bas Draa (Anti-Atlas Occidental, Maroc). *Comptes Rendus L'academie Sci.—Ser. IIa Sci. La Terre Des Planetes* **1998**, *327*, 819–826. https://doi.org/10.1016/S1251-8050(99)80056-1.
40. Walsh, G.J.; Aleinikoff, J.N.; Benziane, F.; Yazidi, A.; Armstrong, T.R. U-Pb Zircon Geochronology of the Paleoproterozoic Tagragra de Tata Inlier and Its Neoproterozoic Cover, Western Anti-Atlas, Morocco. *Precambrian Res.* **2002**, *117*, 1–20. https://doi.org/10.1016/S0301-9268(02)00044-X.
41. Gasquet, D.; Chevremont, P.; Baudin, T.; Chalot-Prat, F.; Guerrot, C.; Cocherie, A.; Roger, J.; Hassenforder, B.; Cheilletz, A. Polycyclic Magmatism in the Tagragra d'Akka and Kerdous-Tafeltast Inliers (Western Anti-Atlas, Morocco). *J. Afr. Earth Sci.* **2004**, *39*, 267–275. https://doi.org/10.1016/j.jafrearsci.2004.07.062.
42. O'Connor, E.; Barnes, R.; Beddoe-Stephens, B.; Fletcher, T.; Gillespie, M.; Hawkins, M.; Loughlin, S.; Smith, M.; Smith, R.; Waters, C. *Geology of the Drâa, Kerdous, and Boumalne districts, Anti-Atlas, Morocco*; British Geological Survey: Nottingham, UK, 2010; p. 310
43. Kouyaté, D.; Söderlund, U.; Youbi, N.; Ernst, R.; Hafid, A.; Ikenne, M.; Soulaimani, A.; Bertrand, H.; El Janati, M.; R'kha Chaham, K. U-Pb Baddeleyite and Zircon Ages of 2040 Ma, 1650 Ma and 885 Ma on Dolerites in the West African Craton (Anti-Atlas Inliers): Possible Links to Break-up of Precambrian Supercontinents. *Lithos* **2013**, *174*, 71–84. https://doi.org/10.1016/j.lithos.2012.04.028.
44. Youbi, N.; Kouyaté, D.; Söderlund, U.; Ernst, R.E.; Soulaimani, A.; Hafid, A.; Ikenne, M.; El Bahat, A.; Bertrand, H.; Chaham, K.R. The 1750 Ma Magmatic Event of the West African Craton (Anti-Atlas, Morocco). *Precambrian Res.* **2013**, *236*, 106–123. https://doi.org/10.1016/j.precamres.2013.07.003.

45. El Bahat, A.; Ikenne, M.; Söderlund, U.; Cousens, B.; Youbi, N.; Ernst, R.; Soulaimani, A.; El Janati, M.; Hafid, A. U-Pb Baddeleyite Ages and Geochemistry of Dolerite Dykes in the Bas Drâa Inlier of the Anti-Atlas of Morocco: Newly Identified 1380 Ma Event in the West African Craton. *Lithos* **2013**, *174*, 85–98. https://doi.org/10.1016/j.lithos.2012.07.022.
46. El Bahat, A.; Ikenne, M.; Cousens, B.; Söderlund, U.; Ernst, R.; Klausen, M.B.; Youbi, N. New Constraints on the Geochronology and Sm-Nd Isotopic Characteristics of Bas-Drâa Mafic Dykes, Anti-Atlas of Morocco. *J. Afr. Earth Sci.* **2017**, *127*, 77–87. https://doi.org/10.1016/j.jafrearsci.2016.09.003.
47. Bleeker, W. The Late Archean Record: A Puzzle in ca. 35 Pieces. *Lithos* **2003**, *71*, 99–134. https://doi.org/10.1016/j.lithos.2003.07.003.
48. Ernst, R.E.; Bleeker, W.; Söderlund, U.; Kerr, A.C. Large Igneous Provinces and Supercontinents: Toward Completing the Plate Tectonic Revolution. *Lithos* **2013**, *174*, 1–14. https://doi.org/10.1016/j.lithos.2013.02.017.
49. Maloof, A.C.; Schrag, D.P.; Crowley, J.L.; Bowring, S.A. An Expanded Record of Early Cambrian Carbon Cycling from the Anti-Atlas Margin, Morocco. *Can. J. Earth Sci.* **2005**, *42*, 2195–2216. https://doi.org/10.1139/e05-062.
50. Ernst, R.E.; Youbi, N. How Large Igneous Provinces Affect Global Climate, Sometimes Cause Mass Extinctions, and Represent Natural Markers in the Geological Record. *Palaeogeogr. Palaeoclimatol. Palaeoecol.* **2017**, *478*, 30–52. https://doi.org/10.1016/j.palaeo.2017.03.014.
51. Álvaro, J.J.; Pouclet, A.; Ezzouhairi, H.; Soulaimani, A.; Bouougri, E.H.; Imaz, A.G.; Fekkak, A. Early Neoproterozoic Rift-Related Magmatism in the Anti-Atlas Margin of the West African Craton, Morocco. *Precambrian Res.* **2014**, *255*, 433–442. https://doi.org/10.1016/j.precamres.2014.10.008.
52. Bouougri, E.H.; Saquaque, A. Lithostratigraphic Framework and Correlation of the Neoproterozoic Northern West African Craton Passive Margin Sequence (Siroua-Zenaga-Bouazzer Elgraara Inliers, Central Anti-Atlas, Morocco): An Integrated Approach. *J. Afr. Earth Sci.* **2004**, *39*, 227–238. https://doi.org/10.1016/j.jafrearsci.2004.07.045.
53. Ait Lahna, A.; Tassinari, C.C.G.; Youbi, N.; Admou, H.; Bouougri, E.H.; Chaib, L.; Ernst, R.E.; Soderlund, U.; Boumehdi, A.; Bensalah, M.K.; et al. Refining the stratigraphy of the taghdout group by using the U–Pb geochronology of the taghdout sill (Zenaga inlier, Anti-Atlas, Morocco). *Acta Geol. Sin.* **2016**, *90*, 1. https://doi.org/10.1111/1755-6724.12846.
54. Bouougri, E.H.; Lahna, A.A.; Tassinari, C.C.G.; Basei, M.A.S.; Youbi, N.; Admou, H.; Saquaque, A.; Boumehdi, M.A.; Maacha, L. Time Constraints on Early Tonian Rifting and Cryogenian Arc Terrane-Continent Convergence along the Northern Margin of the West African Craton: Insights from SHRIMP and LA-ICP-MS Zircon Geochronology in the Pan-African Anti-Atlas Belt (Morocco). *Gondwana Res.* **2020**, *85*, 169–188. https://doi.org/10.1016/j.gr.2020.03.011.
55. El Hadi, H.; Simancas, J.F.; Martínez-Poyatos, D.; Azor, A.; Tahiri, A.; Montero, P.; Fanning, C.M.; Bea, F.; González-Lodeiro, F. Structural and Geochronological Constraints on the Evolution of the Bou Azzer Neoproterozoic Ophiolite (Anti-Atlas, Morocco). *Precambrian Res.* **2010**, *182*, 1–14. https://doi.org/10.1016/j.precamres.2010.06.011.
56. Leblanc, M. Ophiolites Précambriennes et Gites Arseniés de Cobalt: Bou Azzer (Maroc). Ph.D. Thesis, Faculté des Sciences, Université Paris VI, Mémoires du Centre de Géologie et de Géophysique, Paris, France, 1975, p. 329.
57. Leblanc, M. The Late Proterozoic Ophiolites of Bou Azzer (Morocco): Evidence for Pan-African Plate Tectonics. *Dev. Precambrian Geol.* **1981**, *4*, 435–451. https://doi.org/10.1016/S0166-2635(08)70022-7.
58. Admou, H.; Juteau, T. Découverte d'un Système Hydrothermal Océanique Fossile Dans l'ophiolite Antécambrienne de Khzama (Massif Du Siroua, Anti-Atlas Marocain). *Comptes Rendus L'académie Des Sci. IIA-Earth Planet. Sci.* **1998**, *327*, 335–340.
59. Chaib, L.; Lahna, A.A.; Admou, H.; Youbi, N.; El Moume, W.; Tassinari, C.C.G.; Mata, J.; Basei, M.A.S.; Sato, K.; Marzoli, A.; et al. Geochemistry and Geochronology of the Neoproterozoic Backarc Basin Khzama Ophiolite (Anti-Atlas Mountains, Morocco): Tectonomagmatic Implications. *Minerals* **2021**, *11*, 56. https://doi.org/10.3390/min11010056.
60. Bodinier, J.L.; Dupuy, C.; Dostal, J. Geochemistry of Precambrian Ophiolites from Bou Azzer, Morocco. *Contrib. Mineral. Petrol.* **1984**, *87*, 43–50. https://doi.org/10.1007/BF00371401.
61. Naidoo, D.D.; Bloomer, S.H.; Saquaque, A.; Hefferan, K. Geochemistry and Significance of Metavolcanic Rocks from the Bou Azzer-El Graara Ophiolite (Morocco). *Precambrian Res.* **1991**, *53*, 79–97. https://doi.org/10.1016/0301-9268(91)90006-V.
62. Ahmed, A.H.; Arai, S.; Abdel-Aziz, Y.M.; Rahimi, A. Spinel Composition as a Petrogenetic Indicator of the Mantle Section in the Neoproterozoic Bou Azzer Ophiolite, Anti-Atlas, Morocco. *Precambrian Res.* **2005**, *138*, 225–234. https://doi.org/10.1016/j.precamres.2005.05.004.
63. Hodel, F.; Macouin, M.; Triantafyllou, A.; Carlut, J.; Berger, J.; Rousse, S.; Ennih, N.; Trindade, R.I.F. Unusual Massive Magnetite Veins and Highly Altered Cr-Spinels as Relics of a Cl-Rich Acidic Hydrothermal Event in Neoproterozoic Serpentinites (Bou Azzer Ophiolite, Anti-Atlas, Morocco). *Precambrian Res.* **2017**, *300*, 151–167. https://doi.org/10.1016/j.precamres.2017.08.005.

64. Triantafyllou, A.; Hodel, F.; Berger, J.; Macouin, M.; Baele, J.-M.; Mattielli, N.; Monnier, C.; Ducea, M.N.; Poujol, M. The Bou Azzer and Sirwa Ophiolites (Anti-Atlas, Morocco): Insight into Polyphased Subduction-Accretion Dynamics During Neoproterozoic Times. In Proceedings of the GSA Annual Meeting, Phoenix, AZ, USA, 22–25 September 2019; Volume 51. https://doi.org/10.1130/abs/2019AM-336212.
65. Triantafyllou, A.; Berger, J.; Baele, J.M.; Mattielli, N.; Ducea, M.N.; Sterckx, S.; Samson, S.; Hodel, F.; Ennih, N. Episodic Magmatism during the Growth of a Neoproterozoic Oceanic Arc (Anti-Atlas, Morocco). *Precambrian Res.* **2020**, *339*, 105610. https://doi.org/10.1016/j.precamres.2020.105610.
66. 66. Pujol-Solà, N.; Proenza, J.A.; Cambeses, A.; Haissen, F.; Escalona-Orellana, H.; Domínguez-Carretero, D.; Novo-Fernández, I.; Arenas, R.; Maacha, L.; Ikenne, M. Petrogenesis of Ultramafic Rocks from the Neoproterozoic Bou Azzer Ophiolite (Morocco): New Insights into a Long-Standing Geodynamic Question. International Geology Review,2024. https://doi.org/10.1080/00206814.2024.2405943.
67. Samson, S.D.; Inglis, J.D.; D'Lemos, R.S.; Admou, H.; Blichert-Toft, J.; Hefferan, K. Geochronological, Geochemical, and Nd-Hf Isotopic Constraints on the Origin of Neoproterozoic Plagiogranites in the Tasriwine Ophiolite, Anti-Atlas Orogen, Morocco. *Precambrian Res.* **2004**, *135*, 133–147. https://doi.org/10.1016/j.precamres.2004.08.003.
68. Triantafyllou, A. Evolution Géodynamique d'un arc Insulaire Néoprotérozoïque de l'Anti-Atlas Marocain: Caractérisation des Processus de Croissance Intra-Océanique et d'accrétion. Ph.D. Thesis, Université de Nantes, Nantes, France, 2015.
69. Triantafyllou, A.; Berger, J.; Baele, J.M.; Diot, H.; Ennih, N.; Plissart, G.; Monnier, C.; Watlet, A.; Bruguier, O.; Spagna, P.; et al. The Tachakoucht-Iriri-Tourtit Arc Complex (Moroccan Anti-Atlas): Neoproterozoic Records of Polyphased Subduction-Accretion Dynamics during the Pan-African Orogeny. *J. Geodyn.* **2016**, *96*, 81–103. https://doi.org/10.1016/j.jog.2015.07.004.
70. Triantafyllou, A.; Berger, J.; Baele, J.M.; Bruguier, O.; Diot, H.; Ennih, N.; Monnier, C.; Plissart, G.; Vandycke, S.; Watlet, A. Intra-Oceanic Arc Growth Driven by Magmatic and Tectonic Processes Recorded in the Neoproterozoic Bougmane Arc Complex (Anti-Atlas, Morocco). *Precambrian Res.* **2018**, *304*, 39–63. https://doi.org/10.1016/j.precamres.2017.10.022.
71. Ouguir, H.; Macaudiere, J.; Dagallier, G.; Qadrouci, A.; Leistel, J.M. Cadre Structural Du Gite Ag-Hg d'Imiter (Anti Atlas, Maroc); Implication Metallogenique. *Bull. La Société Géologique Fr.* **1994**, *165*, 233–248. https://doi.org/10.1016/0148-9062(94)90127-9.
72. Ouguir, H.; Macaudière, J.; Dagallier, G. Le Protérozoïque Supérieur d'Imiter, Saghro Oriental, Maroc: Un Contexte Géodynamique d'arrière-Arc. *J. Afr. Earth Sci.* **1996**, *22*, 173–189. https://doi.org/10.1016/0899-5362(96)00002-4.
73. Benziane, F. Lithostratigraphie et évolution géodynamique de l'anti-Atlas (Maroc) du paléoprotérozoïque aunéoprotérozoïque: Exemples de la boutonnière de Tagragra Tata et du Jebel Saghro. Ph.D. thesis; Université de Chambéry, Chambéry, France, 2007.
74. Abati, J.; Aghzer, A.M.; Gerdes, A.; Ennih, N. Detrital Zircon Ages of Neoproterozoic Sequences of the Moroccan Anti-Atlas Belt. *Precambrian Res.* **2010**, *181*, 115–128. https://doi.org/10.1016/j.precamres.2010.05.018.
75. Michard, A.; Soulaimani, A.; Ouanaimi, H.; Raddi, Y.; Aït Brahim, L.; Rjimati, E.C.; Baidder, L.; Saddiqi, O. Saghro Group in the Ougnat Massif (Morocco), an Evidence for a Continuous Cadomian Basin along the Northern West African Craton. *Comptes Rendus—Geosci.* **2017**, *349*, 81–90. https://doi.org/10.1016/j.crte.2017.01.001.
76. Errami, E.; Linnemann, U.; Hofmann, M.; Gärtner, A.; Zieger, J.; Gärtner, J.; Mende, K.; El Kabouri, J.; Gasquet, G.; Ennih, N. From panafrican transpression to cadomian transtension at the west african margin: New U-Pb zircon ages from the eastern Saghro inlier (Anti-Atlas, Morocco). *Geol. Soc. Lond. Spec. Publ.* **2020**, *503*, 209–233 https://doi.org/10.1144/sp503-2020-105.
77. Karaoui, A.; Breitkreuz, C.; Karaoui, B.; Yajioui, Z.; Mahmoudi, A. Facies Architecture, Modal Analysis and Geochemistry of the Early Ediacaran Turbiditic Series in the Skoura Inlier (Central High Atlas, Morocco): Implications for Provenance and Geotectonic Setting. *J. Afr. Earth Sci.* **2022**, *185*, 104390. https://doi.org/10.1016/j.jafrearsci.2021.104390.
78. Karaoui, A.; Linnemann, U.; Breitkreuz, C.; Karaoui, B.; Yajioui, Z.; Mahmoudi, A.; Zieger-Hofmann, M.; Gärtner, J.; Zieger, J.; Gärtner, A.; et al. Coupled U-Hf Isotopes and Trace Elements of Detrital Zircon Grains from the Lower Ediacaran Turbidites in the Skoura Inlier (Central High Atlas, Morocco): Implications for Crustal Evolution of the North-Western Gondwana Margin. *Precambrian Res.* **2023**, *384*, 106935. https://doi.org/10.1016/j.precamres.2022.106935.
79. Saquaque, A.; Benharref, M.; Abia, H.; Mrini, Z.; Reuber, I.; Karson, J.A. Evidence for a Panafrican Volcanic Arc and Wrench Fault Tectonics in the Jbel Saghro, Anti-Atlas, Morocco. *Geol. Rundsch.* **1992**, *81*, 1–13. https://doi.org/10.1007/BF01764536.
80. Fekkak, A.; Pouclet, A.; Ouguir, H.; Ouazzani, H.; Badra, L.; Gasquet, D. Géochimie et Signification Géotectonique Des Volcanites Du Cryogénien Inférieur Du Saghro (Anti-Atlas Oriental, Maroc)/Geochemistry and Geotectonic Significance of Early Cryogenian Volcanics of Saghro (Eastern Anti-Atlas, Morocco). *Geodin. Acta* **2001**, *14*, 373–385. https://doi.org/10.1080/09853111.2001.10510730.

81. Fekkak, A.; Pouclet, A.; Badra, L. The Pre-Pan-African Rifting of Saghro (Anti-Atlas, Morocco): Example of the Middle Neoproterozoic Basin of Boumalne. *Bull. La Société Géologique Fr.* **2002**, *173*, 25–35. https://doi.org/10.2113/173.1.25.
82. Marini, F.; OUGUIR, H. Un Nouveau Jalon Dans l'histoire de La Distension Pré-Panafricaine Au Maroc: Le Précambrien II Des Boutonnières Du Jbel Saghro Nord-Oriental (Anti-Atlas, Maroc). *Comptes Rendus L'académie Des Sci. Série 2 Mécanique Phys. Chim. Sci. L'univers Sci. La Terre* **1990**, *310*, 577–582.
83. Hefferan, K.; Soulaimani, A.; Samson, S.D.; Admou, H.; Inglis, J.; Saquaque, A.; Latifa, C.; Heywood, N. A Reconsideration of Pan African Orogenic Cycle in the Anti-Atlas Mountains, Morocco. *J. Afr. Earth Sci.* **2014**, *98*, 34–46. https://doi.org/10.1016/j.jafrearsci.2014.03.007.
84. Geyer, G.; Landing, E. Cambrian Deposition in Northwestern Africa: Relationship of Tamlelt Massif (Moroccan–Algerian Border Region) Succession to the Moroccan Meseta. *J. Afr. Earth Sci.* **2020**, *165*, 103772. https://doi.org/10.1016/j.jafrearsci.2020.103772.
85. Ouabid, M.; Garrido, C.J. Widespread Cadomian–Pan-African Ediacaran Magmatism across the Moroccan Meseta: Implication for the Geodynamic Evolution of the NW Gondwana Margin. *Precambrian Res.* **2023**, *387*, 106992. https://doi.org/10.1016/j.precamres.2023.106992.
86. Karaoui, B.; Breitkreuz, C.; Mahmoudi, A.; Youbi, N. Physical Volcanology, Geochemistry and Basin Evolution of the Ediacaran Volcano-Sedimentary Succession in the Bas Draâ Inlier (Ouarzazate Supergroup, Western Anti-Atlas, Morocco). *J. African Earth Sci.* **2014**, *99*, 307–331. https://doi.org/10.1016/j.jafrearsci.2014.06.022.
87. Karaoui, B.; Breitkreuz, C.; Mahmoudi, A.; Youbi, N.; Hofmann, M.; Gärtner, A.; Linnemann, U. U-Pb Zircon Ages from Volcanic and Sedimentary Rocks of the Ediacaran Bas Draâ Inlier (Anti-Atlas Morocco): Chronostratigraphic and Provenance Implications. *Precambrian Res.* **2015**, *263*, 43–58. https://doi.org/10.1016/j.precamres.2015.03.003.
88. Geyer, G.; Landing, E. Ediacaran–Cambrian depositional environments and stratigraphy of the western Atlas Regions, Morocco. UCL Maghreb Petroleum Research Group (MPRG) Infracambrian/ Early Palaeozoic Field Guide Series No. 1. *Beringeria* **2006**, *6*, 47–112.
89. Condon, D.J.; Schoene, B.; McLean, N.M.; Bowring, S.A.; Parrish, R.R. Metrology and Traceability of U-Pb Isotope Dilution Geochronology (EARTHTIME Tracer Calibration Part I). *Geochim. Cosmochim. Acta* **2015**, *164*, 464–480. https://doi.org/10.1016/j.gca.2015.05.026.
90. McLean, N.M.; Condon, D.J.; Schoene, B.; Bowring, S.A. Evaluating Uncertainties in the Calibration of Isotopic Reference Materials and Multi-Element Isotopic Tracers (EARTHTIME Tracer Calibration Part II). *Geochim. Cosmochim. Acta* **2015**, *164*, 481–501. https://doi.org/10.1016/j.gca.2015.02.040.
91. Krogh, T.E. A Low-Contamination Method for Hydrothermal Decomposition of Zircon and Extraction of U and Pb for Isotopic Age Determinations. *Geochim. Cosmochim. Acta* **1973**, *87*, 485–494.
92. Gerstenberger, H.; Haase, G. A Highly Effective Emitter Substance for Mass Spectrometric Pb Isotope Ratio Determinations. *Chem. Geol.* **1997**, *136*, 309–312. https://doi.org/10.1016/S0009-2541(96)00033-2.
93. Von Quadt, A.; Wotzlaw, J.F.; Buret, Y.; Large, S.J.E.; Peytcheva, I.; Trinquier, A. High-Precision Zircon U/Pb Geochronology by ID-TIMS Using New 1013 Ohm Resistors. *J. Anal. At. Spectrom.* **2016**, *31*, 658–665. https://doi.org/10.1039/c5ja00457h.
94. Wotzlaw, J.F.; Buret, Y.; Large, S.J.E.; Szymanowski, D.; Von Quadt, A. ID-TIMS U-Pb Geochronology at the 0.1‰ Level Using 1013 Ω Resistors and Simultaneous U and $^{18}O/^{16}O$ Isotope Ratio Determination for Accurate UO_2 Interference Correction. *J. Anal. At. Spectrom.* **2017**, *32*, 579–586. https://doi.org/10.1039/c6ja00278a.
95. Hiess, J.; Condon, D.J.; McLean, N.; Noble, S.R. $^{238}U/^{235}U$ Systematics in Terrestrial Uranium-Bearing Minerals. *Science* **2012**, *335*, 1610–1614. https://doi.org/10.1126/science.1215507.
96. Bowring, J.F.; McLean, N.M.; Bowring, S.A. Engineering Cyber Infrastructure for U-Pb Geochronology: Tripoli and U-Pb-Redux. Geochemistry, Geophys. *Geosystems* **2012**, *12*, 6. https://doi.org/10.1029/2010GC003479.
97. Ben Chra, M. Etude Du Volcanisme Du Néo-Protérozoïque Terminal de La Boutonnière d'Aguerzoula-Bachkoune, Anti-Atlas Central (Maroc): Lithostratigraphie, Pétrographie, Géochimie et Implications Géodynamiques. Ph.D. thesis, Faculty of Sceinces Semlalia, University Cadi Ayyad, Marrakesh, Morocco, 1997; 231p.
98. El Khanchaoui, T. Atlas Central, Maroc. Lithostratigraphie, Pétrographie, Minéralogie et Géochimie. Ph.D. thesis, Faculty of Sceinces Semlalia, University Cadi Ayyad, Marrakesh, Morocco, 1990; 200p.
99. Diallo, A A. E Etude du Volcanisme du Precambrien Terminal dans la Région de Tinzaline Est du Siroua, Anti-Atlas Central, Maroc. Lithostratigraphie, Pétrographie et Géochimie. Ph.D. thesis, Faculty of Sceinces Semlalia, University Cadi Ayyad, Marrakesh, Morocco, 1989; 224p..

100. Chayla, B.; Jaffrezic, H.; Joron, J.-L. Analyse par activation neutronique dans les neutrons épithermiques. Application à la détermination d'éléments en traces dans les roches. *C.R. Acad. Sci*. **1973**, *227*, 273–275.
101. De la Roche, H.; Govindaraju, K. Nouveaux Étalons Géochimiques: Granite GS-N et Feldspath FK-N. *Analusis* **1976**, *4*, 347–372.
102. Govindaraju, K. Report on Three GIT-IWG Rock Reference Samples: Anorthosite from Greenland, AN-G.; Basalte d'Essey-la-Côte, BE-N.; Granite de Beauvoir, MA-N. *Geostand. Newsl.* **1980**, *4*, 49–138. https://doi.org/10.1111/j.1751-908X.1980.tb00274.x.
103. Winchester, J.A.; Floyd, P.A. Geochemical Discrimination of Different Magma Series and Their Differentiation Products Using Immobile Elements. *Chem. Geol.* **1977**, *20*, 325–343. https://doi.org/10.1016/0009-2541(77)90057-2.
104. Masuda, A.; Nakamura, N.; Tanaka, T. Fine Structures of Mutually Normalized Rare-Earth Patterns of Chondrites. *Geochim. Cosmochim. Acta* **1973**, *37*, 239–248. https://doi.org/10.1016/0016-7037(73)90131-2.
105. Sun, S.S.; McDonough, W.F. Chemical and Isotopic Systematics of Oceanic Basalts: Implications for Mantle Composition and Processes. *Geol. Soc. Spec. Publ.* **1989**, *42*, 313–345. https://doi.org/10.1144/GSL.SP.1989.042.01.19.
106. Shand, S.J. *Eruptive Rocks: Their Genesis, Classification, and Their Relation to Ore Deposits, with a Chapter on Meteorites*; John Wiley and Sons: New York, NY, USA, 1951.
107. Maniar, P.D.; Piccoli, P.M. Tectonic Discrimination of Granitoids. *Geol. Soc. Am. Bull.* **1989**, *101*, 635–643. https://doi.org/10.1130/0016-7606(1989)101<0635:TDOG>2.3.CO;2.
108. Leat, P.T.; Jackson, S.E.; Thorpe, R.S.; Stillman, C.J. Geochemistry of Bimodal Basalt-Subalkaline/Peralkaline Rhyolite Provinces Within the Southern British Caledonides. *J. Geol. Soc. London.* **1986**, *143*, 259–273. https://doi.org/10.1144/gsjgs.143.2.0259.
109. Poldervaart, A.; Hess, H.H. Pyroxenes in the Crystallization of Basaltic Magma. *J. Geol.* **1951**, *59*, 472–489. https://doi.org/10.1086/625891.
110. Leterrier, J.; Maury, R.C.; Thonon, P.; Girard, D.; Marchal, M. Clinopyroxene Composition as a Method of Identification of the Magmatic Affinities of Paleo-Volcanic Series. *Earth Planet. Sci. Lett.* **1982**, *59*, 139–154. https://doi.org/10.1016/0012-821X(82)90122-4.
111. Cas, R.A.F.; Wright, J. Volcanic Successions. Modern and Ancient. In *A geological Approach to Processes, Products and Successions*; Chapman and Hall: London, UK,1987; 528p.
112. Chatir, A. Caractérisations et Modèle de Formation Du Gisement de Talc de Nkob (Anti-Atlas Marocain) Caractérisations et modèle de formation du gisement de Talc de Nkob (Anti-Atlas marocain). Sciences de la Terre. Ph.D. thesis; Université Chouaïb Doukkali, El Jadida, Morocco, 2022, p393.
113. Saïd, B.; Perrot, M.; Davies, J.H.F.L.; Liégeois, J.-P.; Ikenne, M. The Ediacaran Ouarzazate Group, a Metacratonic Silicic Large Igneous Province (Slip): New U-Pb Zircon Ages From Ouzellarh-Siroua Salient (Tifnoute Valley). In Proceedings of the 56th Annual Meeting, Tucson, AZ, USA, 25–28 October 2021; pp. 1–2. https://doi.org/10.1130/abs/2021ne-361648.
114. Toummite, A.; Liegeois, J.P.; Gasquet, D.; Bruguier, O.; Beraaouz, E.H.; Ikenne, M. Field, Geochemistry and Sr-Nd Isotopes of the Pan-African Granitoids from the Tifnoute Valley (Sirwa, Anti-Atlas, Morocco): A Post-Collisional Event in a Metacratonic Setting. *Mineral. Petrol.* **2013**, *107*, 739–763. https://doi.org/10.1007/s00710-012-0245-3.
115. El Moume, W.; Youbi, N.; Marzoli, A.; Bertrand, H.; Ikenne, M.; Boumehdi, M.A.; Ernst, R.; El Hachimi, H.; Bensalah, M.K.; Mata, J. Geochemistry of Mafic Dyke Swarms of Douar Eç-Çour (High Atlas, Morocco): The Farthest Record of the Central Iapetus Magmatic Province (CIMP) into West African Craton. *GEONOVAS* **2020**, *33*, 95–124.
116. Condon, D.J.; Bowring, S.A. *Chapter 9 A User's Guide to Neoproterozoic Geochronology*; The Geological Society of London: London, UK, 2011; Volume 36. https://doi.org/10.1144/m36.9.
117. Shaw, D.M. *Trace Elements in Magmas: A Theoretical Treatment*; Cambridge University Press: Cambridge, UK, 2006. https://doi.org/10.1017/S0016756808004652.
118. Whittington, D. Mesozoic Diabase Dikes of North Carolina. Ph.D. Dissertation, The Florida State University, College of Arts and Sciences, FL, USA, 1988; pp. 147–199.
119. Whittington, D. Chemical and Physical Constraints on Petrogenesis and Emplacement of ENA Olivine Diabase Magma Types. In *Triassic-Jurassic Rifting: Continental Breakup and the Origin of the Atlantic Ocean and Passive Margins*; Developments in Geotectonics 22; Elsevier: Amsterdam, The Netherlands, 1988; Volume 22, pp. 557–577.
120. Wilson, M. Igneous Petrogenesis; A Global Tectonic Approach; London: Unwin Hyman, London, UK, 1989; pp. 101–50. doi.org/10.1007/978-1-4020-6788-4_5.
121. Allègre, C.J.; Treuil, M.; Minster, J.-F.; Minster, B.; Albarède, F. Systematic Use of Trace Element in Igneous Process: Part I: Fractional Crystallization Processes in Volcanic Suites. Contrib. to Mineral. Petrol. 1977, 60, 57–75. . https://doi.org/10.1007/BF00372851/METRICS

122. Joron, J.L.; Treuil, M. Hygromagmaphile Element Distributions in Oceanic Basalts as Fingerprints of Partial Melting and Mantle Heterogeneities: A Specific Approach and Proposal of an Identification and Modelling Method. *Geol. Soc. Spec. Publ.* **1989**, *42*, 277–299. https://doi.org/10.1144/GSL.SP.1989.042.01.17.
123. Pearce, J.A. Trace Element Characteristics of Lavas from Destructive Plate Boundaries. In: Thorpe, R.S. (ed.). Orogenic Andesites and Related Rocks; John Wiley and Sons: Hoboken, NJ, USA, 1982; pp. 528–548.
124. Cabanis, B.; Thieblemont, D. La Discrimination Des Tholeiites Continentales et Des Basaltes Arriere-Arc; Proposition d'un Nouveau Diagramme, Le Triangle Th-3xTb-2xTa. Bull. *La Société Géologique Fr.* **1988**, *4*, 927–935.
125. Hagemann, S.G.; Cassidy, K.F. *Archean Orogenic Lode Gold Deposits. Archaean lode gold deposits: Reviews in Economic Geology*; Society of Economic Geologists: Littleton, CO, USA, 2000; Volume 13, pp. 9–68.
126. Cabanis, , B. Identification Des Séries Magmatiques Dans Les Socles Métamorphiques Sur La Base de Critères Géologiques, Pétrographiques et Géochimiques; Mémoire des Sciences de la Terre, Université Pierre et Marie Curie, Paris, France, 1986; pp. 74–86.
127. Rollinson, H.R. Using Geochemical Data: Evaluation. *Present. Interpret.* **1993**, *796*, 317. https://doi.org/10.4324/9781315845548.
128. Hofmann, A.W.; Jochum, K.P.; Seufert, M.; White, W.M. Nb and Pb in Oceanic Basalts: New Constraints on Mantle Evolution. *Earth Planet. Sci. Lett.* **1986**, *79*, 33–45. https://doi.org/10.1016/0012-821X(86)90038-5.
129. Hofmann, A.W.; Class, C.; Goldstein, S.L. Size and Composition of the MORB + OIB Mantle Reservoir. *Geochem. Geophys. Geosystems* **2022**, *23*, e2022GC010339. https://doi.org/10.1029/2022GC010339.
130. Rudnick, R.; Gao, S - Composition of the Continental Crust. In: Holland, H.D., Turekian, K.K. (Eds.), Treatise on Geochemistry. Pergamon, Oxford, 2003, Volume 3, pp. 1–64. https://doi.org/10.1016/B0-08-043751-6/03016-4.
131. Baier, J.; Audétat, A.; Keppler, H. The Origin of the Negative Niobium Tantalum Anomaly in Subduction Zone Magmas. *Earth Planet. Sci. Lett.* **2008**, *267*, 290–300. https://doi.org/10.1016/j.epsl.2007.11.032.
132. Rustioni, G.; Audetat, A.; Keppler, H. The Composition of Subduction Zone Fluids and the Origin of the Trace Element Enrichment in Arc Magmas. *Contrib. Mineral. Petrol.* **2021**, *176*, 51. https://doi.org/10.1007/s00410-021-01810-8.
133. Pearce, J.A. Geochemical Fingerprinting of Oceanic Basalts with Applications to Ophiolite Classification and the Search for Archean Oceanic Crust. *Lithos* **2008**, *100*, 14–48. https://doi.org/10.1016/j.lithos.2007.06.016.
134. Kovalenko, V.I.; Naumov, V.B.; Girnis, A.V.; Dorofeeva, V.A.; Yarmolyuk, V. V Average Composition of Basic Magmas and Mantle Sources of Island Arcs and Active Continental Margins Estimated from the Data on Melt Inclusions and Quenched Glasses of Rocks. *Petrology* **2010**, *18*, 1–26. https://doi.org/10.1134/S0869591110010017.
135. Stern, R.J. Subduction Zones. *Rev. Geophys.* **2002**, *40*, 3-1–3-38. https://doi.org/10.1029/2001RG000108.
136. Jagoutz, O.; Kelemen, P.B. Role of Arc Processes in the Formation of Continental Crust. *Annu. Rev. Earth Planet. Sci.* **2015**, *43*, 363–404. https://doi.org/10.1146/annurev-earth-040809-152345.
137. Zhu, D.-C.; Wang, Q.; Weinberg, R.F.; Cawood, P.A.; Chung, S.-L.; Zheng, Y.-F.; Zhao, Z.; Hou, Z.-Q.; Mo, X.-X. Interplay Between Oceanic Subduction and Continental Collision in Building Continental Crust. *Nat. Commun.* **2022**, *13*, 7141. https://doi.org/10.1038/s41467-022-34826-0.
138. Rudnick, R.L.; Gao, S. *Composition of the Continental Crust*, 2nd ed.; Elsevier Ltd.: Amsterdam, The Netherlands, 2013; Volume 4.://doi.org/10.1016/B0-08-043751-6/03016-4.
139. Cai, R.; Liu, J.; Sun, Y.; Gao, R. Phosphorus Deficit in Continental Crust Induced by Recycling of Apatite-Bearing Cumulates. *Geology* **2023**, *51*, 500–504. https://doi.org/10.1130/G51027.1.
140. McKenzie, D.A.N.; O'nions, R.K. Partial Melt Distributions from Inversion of Rare Earth Element Concentrations. *J. Petrol.* **1991**, *32*, 1021–1091. https://doi.org/10.1093/petrology/32.5.1021.
141. Johnson, K.T.M. Experimental Cpx/and Garnet/Melt Partitioning of REE and Other Trace Elements at High Pressures: Petrogenetic Implications. *Mineral. Mag. A* **1994**, *58*, 454–455.
142. Gaetani, G.A.; Kent, A.J.R.; Grove, T.L.; Hutcheon, I.D.; Stolper, E.M. Mineral/Melt Partitioning of Trace Elements during Hydrous Peridotite Partial Melting. *Contrib. Mineral. Petrol.* **2003**, *145*, 391–405. https://doi.org/10.1007/s00410-003-0447-0.
143. Ellam, R.M. Lithospheric Thickness as a Control on Basalt Geochemistry. *Geology* **1992**, *20*, 153–156. https://doi.org/10.1130/0091-7613(1992)020<0153:LTAACO>2.3.CO;2.
144. Fitton, J.G.; James, D.; Kempton, P.D.; Ormerod, D.S.; Leeman, W.P. The Role of Lithospheric Mantle in the Generation of Late Cenozoic Basic Magmas in the Western United States. *J. Petrol.* **1988**, *Special_Volume*,1, 331–349. https://doi.org/10.1093/petrology/Special_Volume.1.331.

145. Leat, P.T.; Thompson, R.N.; Morrison, M.A.; Hendry, G.L.; Dickin, A.P. Compositionally-Diverse Miocene-Recent Rift-Related Magmatism in Northwest Colorado: Partial Melting, and Mixing of Mafic Magmas from 3 Different Asthenospheric and Lithospheric Mantle Sources. *J. Petrol.* **1988**, *Special_Volume*, *1*, 351–377. https://doi.org/10.1093/petrology/Special_Volume.1.351.
146. Thompson, R.N.; Morrison, M.A. Asthenospheric and Lower-Lithospheric Mantle Contributions to Continental Extensional Magmatism: An Example from the British Tertiary Province. *Chem. Geol.* **1988**, *68*, 1–15. https://doi.org/10.1016/0009-2541(88)90082-4.
147. Mckenzie, D.; O'nions, R.K. Corrections to "Partial Melt Distributions from Inversion of Rare Earth Element Concentrations". *J. Petrol.* **1992**, *33*, 1453. https://doi.org/10.1093/petrology/33.6.1453.
148. Klemme, S.; Blundy, J.D.; Wood, B.J. Experimental Constraints on Major and Trace Element Partitioning during Partial Melting of Eclogite. *Geochim. Cosmochim. Acta* **2002**, *66*, 3109–3123. https://doi.org/10.1016/S0016-7037(02)00859-1.
149. Ziberna, L.; Klemme, S.; Nimis, P. Garnet and Spinel in Fertile and Depleted Mantle: Insights from Thermodynamic Modelling. *Contrib. Mineral. Petrol.* **2013**, *166*, 411–421. https://doi.org/10.1007/s00410-013-0882-5.
150. Condie, K.C. High Field Strength Element Ratios in Archean Basalts: A Window to Evolving Sources of Mantle Plumes? *Lithos* **2005**, *79*, 491–504. https://doi.org/10.1016/j.lithos.2004.09.014.
151. Cabanis, B.; Lecolle, M. Le Diagramme La/10.-Y/15-Nb/8: Un Outil Pour La Discrimination de Series Volcaniques et La Mise En Evidence Des Processus de Melange et/Ou de Contamintion Crustale. *Comptes Rendus Lacadmie Des Sci. Srie II. Mcanique Phys. Chim. Sci. Lunivers Sci. La Terre* **1989**, *309*, 20232029.
152. Saunders, A.D.; Storey, M.; Kent, R.W.; Norry, M.J. Consequences of Plume-Lithosphere Interactions. *Geol. Soc. Lond. Spec. Publ.* **1992**, *68*, 41–60. https://doi.org/10.1144/GSL.SP.1992.068.01.04.
153. Kepezhinskas, P.; McDermott, F.; Defant, M.J.; Hochstaedter, A.; Drummond, M.S.; Hawkesworth, C.J.; Koloskov, A.; Maury, R.C.; Bellon, H. Trace Element and Sr Nd Pb Isotopic Constraints on a Three-Component Model of Kamchatka Arc Petrogenesis. *Geochim. Cosmochim. Acta* **1997**, *61*, 577–600. https://doi.org/10.1016/S0016-7037(96)00349-3.
154. Cawood, P.A.; Martin, E.L.; Murphy, J.B.; Pisarevsky, S.A. Gondwana's Interlinked Peripheral Orogens. *Earth Planet. Sci. Lett.* **2021**, *568*, 117057. https://doi.org/10.1016/j.epsl.2021.117057.
155. Cawood, P.A.; Kröner, A.; Collins, W.J.; Kusky, T.M.; Mooney, W.D.; Windley, B.F. Accretionary Orogens through Earth History. *Geol. Soc. Spec. Publ.* **2009**, *318*, 1–36. https://doi.org/10.1144/SP318.1.
156. Stern, R.J. The Cadomian (~550 Ma) Orogen in North Africa and Arabia. *J. Afr. Earth Sci.* **2024**, *215*, 105276. https://doi.org/10.1016/j.jafrearsci.2024.105276.
157. Ikenne, M.; Souhassou, M.; Arai, S.; Soulaimani, A. A Historical Overview of Moroccan Magmatic Events along Northwest Edge of the West African Craton. *J. Afr. Earth Sci.* **2017**, *127*, 3–15. https://doi.org/10.1016/j.jafrearsci.2016.10.002.
158. Soulaimani, A.; Ouanaimi, H.; Saddiqi, O.; Baidder, L.; Michard, A. The Anti-Atlas Pan-African Belt (Morocco): Overview and Pending Questions. *Comptes Rendus—Geosci.* **2018**, *350*, 279–288. https://doi.org/10.1016/j.crte.2018.07.002.
159. Chabane, A. Les roches vertes du Protérozoïque Supérieur de Khzama (Siroua, Anti-Atlas, Maroc): Un exemple d'ophiolite d'avant-arc formé en contexte de tranformante. Ph.D. thesis, Faculty of Sceinces Semlalia, University Cadi Ayyad, Marrakesh, Morocco; 454p.
160. Leblanc, M.; Lancelot, J.R. Interprétation Géodynamique Du Domaine Pan-Africain (Précambrien Terminal) de l'Anti-Atlas (Maroc) à Partir de Données Géologiques et Géochronologiques. *Can. J. Earth Sci.* **1980**, *17*, 142–155. https://doi.org/10.1139/e80-012.
161. Schermerhorn, L. J. G., Wallbrecher, E.; Huch, K. M. Der subduktionskomplex, Granit plutonismus und schertektonik im Grundgebirge des Sirwa-Doms (Anti-Arias, Marokko) Berllner Geowtss. Abh. (A), 1986, v. 88, p 301-332.
162. Brabers, P.; Vogel, D.E. Modèle Géodynamique de l'orogenèse Panafricaine Dans l'Anti-Atlas, Maroc. Proceedings of the 13th Colloquium of African Geology. St. Andrews, Scotland, 10–13 September 1985; Volume 19.
163. Bajja, A. Nouvelles données pétrographiques et géochimiques sur les formations volcaniques précambriennes du Jbel Saghro (Anti-Atlas marocain). Basaltes en coussins du PII et volcanites de la série de Ouarzazate (PIII). Thèse dUniversité de Nancy I, Nancy, France, 1987; 224p.
164. Saquaque, A.; Admou, H.; Karson, J.; Hefferan, K.; Reuber, I. Precambrian Accretionary Tectonics in the Bou Azzer-El Graara Region, Anti-Atlas, Morocco. *Geology* **1989**, *17*, 1107–1110. https://doi.org/10.1130/0091-7613(1989)017<1107:PATITB>2.3.CO;2.
165. Mrini, Z. Chronologie (Rb-Sr, U-Pb), Chronologie (Rb-Sr, U-Pb), Traqage Isotopique (Sr-Nd-Pb) des Sources de Roches Magmatiques Kburnkennes, Panafricaines et Hercyniennes du Maroc. Ph.D. Thesis, Université Cadi Ayad, Marrakech, Morocco,1993; p. 200.

166. Brabers, P.M., Een plaattectonisch model voor de Panfrikaanse orogenese in de Anti-Atlas, Marokko. Ph.D. Thesis, Katholieke Universiteit Leuven, Belgium, **1986.**
167. Brabers, P.M., A plate tectonic model for the Panafrican Orogeny in the Anti-Atlas, Morocco. Lect. Notes Earth Sci. **1988**, p 61–80. https://doi.org/10.1007/bfb0011586.
168. Huch, K.M. Die Panafrikanische Khzama-Geosutur in Zentralen Anti-Atlas Morokko. Petrographie Geochemie und Geochronologie des Subduktions-Komplexes der Tourtit-Ophiolithe und der Tachankacht-Gneise Sowie Einiger Kollisionsgesteine om Nordosten des Sirwa-Kristallindoms. Ph.D. Dissertation, Freie Univesität Berlin, Berlin, Germany; 122p.
169. Rehdorf, K. Geologische und Geochemische Aspekte von Vorlandgesteinen eines Panafrikanischen Subduktions-Komplexes Nordöstlich des Jbel Siroua (Anti-Atlas, Südmarokko). PhD. Thesis, Freie Univesität Berlin: Berlin, Germany; 122p.
170. El Boukhari, A. Magmatisme et Métasediments Associés Du Protérozoïque Supérieur de La Zone de N'Kob (Siroua-Se, Anti-Atlas Central Maroc): Une Ophiolite Formée et Mise En Place Sur La Marge Du Craton Ouest-Africain. Ph.D. thesis, Faculty of Sceinces Semlalia, University Cadi Ayyad, Marrakesh, Morocco, 1991; 511 p.
171. Amaral, J.L.; Mata, J.; Santos, J.F. The Carboniferous Shoshonitic (Sl) Gabbro–Monzonitic Stocks of Veiros and Vale de Maceira, Ossa-Morena Zone (SW Iberian Massif): Evidence for Diverse Subduction-Related Lithospheric Metasomatism. *Geochemistry* **2022**, *82*, 125917; https://doi.org/10.1016/j.chemer.2022.125917.
172. Bird, P. Continental Delamination and the Colorado Plateau. *J. Geophys. Res. Solid Earth* **1979**, *84*, 7561–7571. https://doi.org/10.1029/JB084iB13p07561.
173. Davies, J.H.; von Blanckenburg, F. Slab Breakoff: A Model of Lithosphere Detachment and Its Test in the Magmatism and Deformation of Collisional Orogens. *Earth Planet. Sci. Lett.* **1995**, *129*, 85–102. https://doi.org/10.1016/0012-821X(94)00237-S.
174. Houseman, G.A.; McKenzie, D.P.; Molnar, P. Convective Instability of a Thickened Boundary Layer and Its Relevance for the Thermal Evolution of Continental Convergent Belts. *J. Geophys. Res. Solid Earth* **1981**, *86*, 6115–6132. https://doi.org/10.1029/JB086iB07p06115.
175. Kay, R.W.; Kay, S.M. Delamination and Delamination. *Tectonophysics* **1993**, *219*, 177–189. https://doi.org/10.1016/0040-1951(93)90295-U.
176. Finger, F.; Gerdes, A.; René, M.; Riegler, G. The Saxo-Danubian Granite Belt: Magmatic Response to Post-Collisional Delamination of Mantle Lithosphere below the Southwestern Sector of the Bohemian Massif (Variscan Orogen). *Geol. Carpathica* **2009**, *60*, 205–212. https://doi.org/10.2478/v10096-009-0014-3.
177. Magni, V.; Király, Á. Delamination . In *Reference Module in Earth Systems and Environmental Sciences*; Elsevier: Amsterdam, The Netherlands, 2020; pp. 1–8. https://doi.org/10.1016/B978-0-12-409548-9.09515-4.
178. Fowler, A.R.; Hamimi, Z. Lithospheric Delamination in Models of Post-Collision Tectonics in the Egyptian Eastern Desert and Sinai: Claims versus Evidence. *J. Afr. Earth Sci.* **2023**, *203*, 104948. https://doi.org/10.1016/j.jafrearsci.2023.104948.
179. Ikenne, M.; Souhassou, M.; Cousens, B.; Montero, P.; Bea, F.; Askkour, F.; Haissen, F.; Beraaouz, E.H.; Ernst, R.E.; Bajddi, A.; et al. Zircon U–Pb Geochronology and Sm–Nd and Rb–Sr Isotope Systematics of Neoproterozoic Granitoïds from Bou Azzer (Anti-Atlas-Morocco): The Obduction Trigger of the Central Anti-Atlas Terrane. *J. Afr. Earth Sci.* **2023**, *202*, 104900. https://doi.org/10.1016/j.jafrearsci.2023.104900.
180. Anderson, D.L. Large Igneous Provinces, Delamination, and Fertile Mantle. *Elements* **2005**, *1*, 271–275. https://doi.org/10.2113/gselements.1.5.271.